Spatial and temporal heterogeneity of geochemical controls on carbon cycling in a tidal salt marsh

Authorship:

Angelia L. Seyfferth[1,2]*, Frances Bothfeld[1], Rodrigo Vargas[1], Jason W. Stuckey[1,3], Jian Wang[4], Kelli Kearns[1,5,6], Holly A. Michael[2,5], Julia Guimond[2], Xuan Yu[2,7], Donald L. Sparks[1]

[1]Department of Plant and Soil Sciences, University of Delaware

[2]Department of Geological Sciences, University of Delaware

[3]Department of Biology and Environmental Science Program, Multnomah University

[4]Canadian Light Source Inc., University of Saskatchewan

[5]Department of Civil and Environmental Engineering, University of Delaware

[6]Environmental Resources Management

[7]School of Civil Engineering, Sun Yat-sen University

*Corresponding Author: angelias@udel.edu, 531 S. College Avenue, 152 Townsend Hall, Newark DE USA 19711, Phone: (302)-831-4865

Keywords: CH_4, CO_2, fluxes, STXM-NEXAFS, X-ray diffraction, redox, Fe EXAFS

Abstract

Tidal salt marsh ecosystems store copious amounts of carbon (C) within sediments. In order to predict how these C stores may be affected by environmental change, it is critical to assess current CO_2 and CH_4 production and efflux from these ecosystems. Production and efflux of these greenhouse gases (GHGs) are governed by coupled geochemical, hydrological, physical and biological processes in sediments that are sensitive to local conditions, which can result in large spatial and temporal heterogeneity of GHGs dynamics within the ecosystem. To understand how the drivers of GHGs dynamics vary across salt marsh ecosystems, we coupled solid-phase geochemistry to measurements of porewater chemistry (to ~1 m), CO_2 and CH_4 production in sediments and efflux to the atmosphere in a temperate tidal salt marsh for over one year to capture seasonal patterns within two vegetation zones of the marsh landscape that have distinct biogeochemical and hydrologic conditions: Tall *Spartina* (TS) and Short *Spartina* (SS). The SS vegetation zone experienced nearly constant inundation, low redox values (-200 to 200 mV), porewater pH 6-7 that did not vary with depth or time, an enrichment of pyrite and goethite with depth and up to 3 mM porewater sulfide. In contrast, the TS vegetation zone on the natural levee proximal to a tidal channel experienced large water level oscillations due to spring-neap tides that resulted in variable but higher redox values (0-700 mV), porewater pH 6-7 at depth but surface (0-3 cm) as low as 4 in the spring, an enrichment of ferrihydrite and a depletion of pyrite at ~30 cm, and up to 0.8 mM ferrous Fe in porewater. At 50-56 cm, solid phase analyses (STXM-NEXAFS) revealed differential C speciation between the two vegetation zones, with stronger C-Fe spatial association at TS and stronger C-Ca co-association at SS despite both having similar soil pH of 3 – 4. These results suggest that soil pH may not be strongly predictive of C-mineral control in flooded marsh sediments. Both vegetation zones showed consistent CO_2

48 and CH_4 emissions from sediments to the atmosphere throughout the study period with TS
49 having ~60% higher median CO_2 and SS having ~55% higher median CH_4 efflux. Using depth
50 profiling, unexpectedly high concentrations of CO_2 (>200 μM) and CH_4 (>200 μM) were
51 observed at depths 50-75 cm at both zones that were higher for SS in these sulfate-rich (up to 17
52 mM) sediments, which suggests methylotrophic methanogenesis occurs deep within the profile
53 of salt marsh sediments away from the tidal channel. Moreover, if we extrapolate our median
54 depth values of CH_4 and CO_2 to the 5.3 Mha of global salt marshes, this could account for a
55 conservative estimate of ~70 Gg of unaccounted C stored in gaseous form (i.e., CH_4 and CO_2) in
56 marsh sediments, which should be considered when attempting to understand the current patterns
57 and future responses of carbon dynamics from these ecosystems.
58
59

1. INTRODUCTION

Tidal salt marsh ecosystems store 1-3 orders of magnitude more carbon in sediments (~218 g C m^{-2} yr^{-1}) than freshwater wetlands (20 – 30 g C m^{-2} yr^{-1}) or forests (0.7 – 55 g C m^{-2} yr^{-1}) (Roulet, 2000; Chmura et al., 2003; Mcleod et al., 2011), yet can also release a wide range of carbon dioxide (CO_2, 100 – 10,000 g m^{-2} yr^{-1}) and methane (CH_4, 0.5 - 22 g m^{-2} yr^{-1}) greenhouse gases (GHGs) to the atmosphere (Bartlett et al., 1987; Magenheimer et al., 1996; Liu et al., 2019; Cao et al., 2020). Past research indicated that while salt marshes have sustained efflux of CO_2 to the atmosphere, they may not be substantial sources of CH_4 (Chmura et al., 2003; Poffenbarger et al., 2011) due to the inhibitory effects of bacterial sulfate (SO_4^{2-}) reduction on methanogenesis (Kristjansson et al., 1982; Lovley and Phillips, 1987; Kuivila et al., 1989). Supporting this paradigm is the inverse relationship found between concentrations of porewater sulfate and CH_4 or porewater salinity and CH_4 efflux from variable salinity marshes, with near complete cessation of CH_4 production or efflux above 8 mM sulfate and 15‰ salinity (Poffenbarger et al., 2011). In contrast, others have shown that salinity higher than 9‰ does not necessarily inhibit CH_4 production (King and Wiebe, 1978; Van Der Nat and Middelburg, 2000; Weston et al., 2006; Middelburg et al., 2014; Wilson et al., 2015; Xiao et al., 2018). Emerging evidence from a variety of environments from forests to wetlands supports the idea that the heterogeneity of the soil/sediment environment creates microenvironments that can support seemingly exclusive microbial metabolisms in close proximity to each other (Bethke et al., 2011) and therefore affect biogeochemical processes. Examples include the 'methane paradox' with methanogenic activity occurring in microsites in otherwise oxic soil and water environments (Teh and Silver, 2006; Darling and Gooddy, 2006; Angle et al., 2017), reducing conditions in soil aggregate interiors in otherwise oxic environments (Silver et al., 1999; Pallud et al., 2010;

83 Masue-Slowey et al., 2011; Ying et al., 2013; Keiluweit et al., 2017), and simultaneous sulfate
84 reduction and methanogenesis (Oremland et al., 1982; Senior et al., 1982; Postma and Jakobsen,
85 1996; Mer and Roger, 2010; Segarra et al., 2013).
86 It is becoming clear that while sulfate-reducing bacteria can outcompete methanogens for
87 substrate during hydrogenotrophic and aceticlastic methanogenesis, methylotrophic
88 methanogenesis may be the dominant pathway for CH_4 production in sulfate-rich sediments
89 (Oremland et al., 1982; Xiao et al., 2018; Jones et al., 2019). Methylotrophic methanogenesis can
90 proceed through fermentation of methylated compounds such as methanol, methylsulfides or
91 methylamines, and sulfate-reducing bacteria do not compete for substrate. In fact, sulfate-
92 reducing bacteria and fermentive bacteria have been shown to be synergistic in the breakdown of
93 glycine betaine (GBT) to form trimethylamine (TMA), which can then be used methanogens to
94 form CH_4 (Hippe et al., 1979; Oremland et al., 1982; King, 1984; Jones et al., 2019), but CH_4
95 production can also proceed via direct demethylation of GBT (Watkins et al., 2014; Ticak et al.,
96 2015). Because methanogenesis can co-occur in environments dominated by sulfate reduction,
97 this warrants a closer look at the role of tidal salt marsh ecosystems in CH_4 production and efflux
98 to the atmosphere in the context of local-to-global environmental change (IPCC, 2014; Hayes et
99 al., 2018).
100 Not only is the soil environment heterogeneous on the micro-scale, but tidal marshes are
101 heterogeneous on the ecosystem-scale both spatially and temporally, and this heterogeneity
102 should be considered when modeling multiscale C dynamics. Past research has focused
103 predominantly on discrete measurements of either CO_2 or CH_4 efflux from sediments to the
104 atmosphere in specific areas of tidal marshes (Reid et al., 2013) or at the ecosystem-scale for
105 CO_2 and CH_4 using the eddy covariance technique (Knox et al., 2019). Researchers using these

106 approaches have recognized that there is a need to resolve specific landscape contributions and
107 the underlying biogeochemical processes for CO_2 or CH_4 dynamics (Waddington and Roulet,
108 1996; Fagherazzi et al., 2013; Tong et al., 2013; Reid et al., 2013). Previous studies in peatlands
109 and wetlands found that water table depth is a primary driver of CO_2 and CH_4 production due to
110 the effect of inundation on biogeochemistry, specifically redox conditions (Moore and Dalva,
111 1993; Moore and Roulet, 1993; Kelley et al., 1995; Wachinger et al., 2000; Smith et al., 2003).
112 Peatlands and wetlands have similar water table depth variations (0-60 cm) (Mer and Roger,
113 2010) to tidal salt marshes (Wolanski, 2007). However, water table elevations in tidal marshes
114 fluctuate diurnally due to tidal patterns and can be highly variable across the ecosystem, causing
115 CO_2 and CH_4 production, as well as efflux rates, to have both seasonal and diurnal patterns
116 (Bartlett et al., 1985; Chanton et al., 1989; Kelley et al., 1995; Yang and Chang, 1998; Maher et
117 al., 2015; Villa et al., 2019). Tidal influence is also variable across the marsh landscape due to
118 differences in topography and proximity to tidal channels (Drabsch et al., 1999). Water table
119 variations can range from daily swings in the water table caused by tides (~ 50 cm), to no daily
120 variation in water table (Drabsch et al., 1999; Montalto et al., 2007) depending on the ecological
121 zone within a marsh. However, even in areas with little to no daily variations, there can be longer
122 scale variations caused by spring-neap tidal cycles.
123 Differing water table dynamics across tidal salt marshes lead to spatial heterogeneity of
124 biogeochemical processes that affect CO_2 and CH_4 production and efflux. Tides affect the
125 balance of CO_2 and CH_4 production by impacting microbial activity through changes in
126 dissolved oxygen, dissolved organic carbon (DOC), and terminal electron acceptor (TEA)
127 concentrations in sediment porewaters. For example, the incoming tide is a source of DOC
128 (Hemminga et al., 1992; Hemminga et al., 1993), which provides energy for microbial activity

and is often the rate-limiting component in microbial respiration (Winfrey and Zeikus 1977; Holmer and Kristensen 1999). The incoming tide is also a source of SO_4^{2-} that may locally stimulate sulfate-reducing bacteria (SRB), which may compete with methanogens and therefore result in more CO_2 and less CH_4 production (Weston et al., 2010). Furthermore, the outgoing tide can drain portions of the marsh enough to oxygenate the sediments and 'shock' the microbial activity and allow O_2 to re-oxidize some spent TEAs, and thus replenish the supply of TEAs for microbial respiration (Kelley et al., 1995; Segers, 1998; Smith et al., 2003). During periods of inundation, CO_2 and CH_4 produced within the soil column have limited conduits to escape to the atmosphere through sediment pore spaces, and could become trapped within the soil column, especially if the GHGs are produced below the rooting depth of the dominant vegetation, as aerenchyma can act as a conduit for GHGs to escape (Kludze et al., 1993). However, large water table elevation oscillations may allow trapped GHGs to escape, and tidal pumping may laterally transport dissolved GHGs into tidal channels (Trifunovic et al., 2018). Both dissolved CH_4 and CO_2 concentrations have an inverse relationship with tidal amplitude, indicating a flushing effect with low tide (Beck et al., 2008; Grunwald et al., 2009; Tong et al., 2013; Call et al., 2015). However, these previous studies are limited to dissolved CO_2 and CH_4 near or in tidal channels and do not quantify CO_2 or CH_4 gas production with depth and efflux from sediments across the marsh landscape over seasons. We reason that there is a potential for large CO_2 and CH_4 efflux rates directly from sediments in a marsh during tidal cycles, or tidal pumping events, because the absence of inundation during low tide can allow for GHGs trapped deeper in the sediment profile to rapidly escape to the atmosphere.

Here, we aimed to understand how biogeochemical and water table elevation spatial gradients affect CH_4 and CO_2 production and efflux in a temperate tidal salt marsh. We evaluated

152 the temporal and spatial heterogeneity of biogeochemical cycling of redox-sensitive parameters
153 and CO_2 and CH_4 production and efflux across the tidal marsh landscape. We hypothesized that
154 1) vegetation zones on the natural levee proximal to the tidal channel will have a greater change
155 in water level resulting in more oxidizing sediments than zones farther from the tidal channel;
156 and 2) vegetation zones with greater change in water table elevation will have a higher rate of C
157 efflux than those with less variation in water table elevation. The novelty of this study is that we
158 coupled biometeorological information of CH_4 and CO_2 dynamics with solid-phase
159 geochemistry, hydrologic measurements, and porewater chemistry to provide insights about the
160 biogeochemical controls of C dynamics across a temperate tidal marsh landscape.
161

162 **2. METHODS**

163 **2.1. Site Description**

164 This study took place in the St. Jones Reserve, a coastal estuary southwest of Dover,
165 Delaware (Figure 1). The St. Jones is part of the National Estuarine Research Reserve System
166 (NERRS) and is managed by the Delaware Department of Natural Resources and Environmental
167 Control (DNREC). The St. Jones Reserve is 15.2 km^2 with an 8.8 km stretch of medium salinity
168 (~8-25 ‰) tidal river (Capooci et al., 2019). This river is a tributary of the St. Jones River that
169 drains agricultural land but also experiences tidal inundation from the Delaware Bay, as the St.
170 Jones River is a tributary of the Delaware Bay. This region experiences a temperate climate with
171 average temperature ranging from 0 °C in the winter to 25 °C in the summer with a yearly
172 average temperature of 15 °C, and receives about 100 cm annual precipitation (Figure 2a). High
173 tides occur twice daily with amplitudes ranging from ~1 m to ~1.5 m during neap and spring
174 tides, respectively (Figure 2b).

175 The reserve has continuous monitoring of meteorological data managed by the Delaware
176 Environmental Observation System (DEOS), and water quality data that includes salinity, water
177 temperature, conductivity, pH, turbidity, and dissolved oxygen managed by DNREC. There is
178 also a USGS tidal gauge (01483700) monitoring system approximately 20 km upstream of the
179 mouth of the St. Jones River and managed by the MD-DE-DC Water Science Center Dover
180 office that we used for tidal amplitudes.
181 To capture spatial heterogeneity of the marsh, we focused our study on two vegetation
182 zones (Figure 1) across the marsh landscape: Tall Spartina (TS), proximal to the main tidal
183 channel on the natural levee and dominated by the tall form of *Spartina alterniflora* L. (saltmarsh
184 cordgrass) with patches of *S. cynosuriodes* L. (big cordgrass), and Short Spartina (SS),
185 approximately 70 m from the main tidal channel and dominated by the short form of *S.*
186 *alterniflora* L. with patches of *S. patens L.* (saltmeadow cordgrass).
187
188 **2.2. Sediment Cores and Characterization**
189 A 90 cm sediment core was taken at each zone in June 2014. We found that SS had 5
190 distinct horizons and TS had 3 horizons up to 89 cm depth (Table 1). The sediment cores were
191 sectioned into three sections (0-27, 27-73, 73+ cm) for TS and 5 sections (0-19, 19-38, 38-50,
192 50-66, 66+ cm) for SS corresponding to sediment horizon locations (Figure S1), and each section
193 was heat-sealed inside of gas-impermeable bags outfitted with oxygen scrubbers (Mitsubishi
194 Anaero-Pack-Anaero) during transport to the laboratory.
195 Sediment from each horizon was subsampled for solid phase characterization under
196 anoxic conditions. An intact ~ 1 cm^3 portion of each horizon was dried at ambient laboratory
197 temperature under anoxic conditions and reserved for X-ray imaging and C speciation analysis

198 using STXM-NEXAFS (see Section 2.4). A portion of each horizon was composited and sieved
199 to 2 mm for analysis of pH (1:1 water extraction). A portion of the sieved sample was powdered
200 and used for CNS analysis (Elementar Cube), X-ray diffraction (Bruker), and bulk Fe EXAFS
201 (described in the next section). A portion of the sieved sediment was further sieved to 0.15 mm
202 for ammonium oxalate (AAO) extraction to target poorly-crystalline Fe (McKeague and Day,
203 1966) and further sieved to 0.053 mm for citrate-bicarbonate-dithionite (CBD) extractions to
204 target total free Fe (Mehra, 1958). All extracts were analyzed for total elements using ICP-OES
205 (Thermo Elemental Intrepid II XSP Duo View).
206
207 **2.3. Fe EXAFS**

208 Four powdered sediment samples collected from the SS zone at -7, -30, -50, and -70 cm
209 and three from the TS zone at -10, -30, and -80 cm relative to the sediment surface were used for
210 bulk Fe EXAFS. Bulk Fe EXAFS was conducted at the Stanford Synchrotron Radiation
211 Lightsource on beamline 11-2, which is equipped with a Si 2 2 0 (phi 90) LN2-cooled double
212 crystal monochromator and Kirkpatrick-Baez mirrors. The incident beam was detuned to 50% to
213 minimize harmonics and the energy was calibrated using a standard Fe foil to the first Fe
214 inflection point at 7112 eV. Iron K-edge spectra were obtained from 150 eV below the edge to *k*
215 values of 13 $Å^{-1}$ and fluorescence was monitored with a Lytle detector. Four spectra were
216 obtained per sample and were averaged, background subtracted, normalized, fit with a spline
217 function (*k*-weight = 3). These normalized spectra were fit by linear combination using
218 ferrihydrite, goethite, mackinawite, siderite, pyrite and vivianite as standards (Hansel et al.,
219 2003).
220

221 **2.4. STXM-NEXAFS**

222 Sediment samples at depths of 50 and 56 cm were chosen for STXM-NEXAFS analysis
223 from TS and SS, respectively. Field moist samples that had been sealed under anoxic conditions
224 with oxygen scrubbers (Mitsubishi Anaero-Pack-Anaero) during the transport to the lab were
225 allowed to dry in an anoxic glovebox (95% N_2/5% H_2 atmosphere). Visible roots and plant
226 material were removed by hand. Dry sediments were stored and shipped in an anoxic
227 environment (Mitsubishi Anero-Pack Rectangular Jar) without further alteration in order to
228 assess the natural C-mineral associations of the bulk sediments.

229 In preparation for STXM-NEXAFS analysis, we used established protocols to preserve
230 elemental speciation (Chen et al., 2014; Dynes et al., 2015). Briefly, ~ 1 mg of sediment was
231 mixed with ~ 1 mL of anoxic deionized-distilled water and immediately vortexted for 5-10s. A ~
232 50 µL suspension droplet was immediately placed onto a Si_3N_4 window (100 nm thick), and
233 allowed to dry (<< 1 min) in an anoxic glovebox (N_2 atmosphere). STXM-NEXAFS data
234 collection and analysis was performed on the 10ID-1 spectromicroscopy beamline (Kaznatcheev
235 et al., 2007) at the Canadian Light Source, a 2.9-GeV third-generation synchrotron source,
236 following previous methods (Chen et al., 2014; Chen and Sparks, 2015) with the addition of
237 image sequence scan (i.e., stack) collection for the N 1s and K 2p edges. Stack datasets were
238 collected for specific element edges in the following order: C K-edge, K L-edge, Ca L-edge, N
239 K-edge, Fe L-edge, Al K-edge, and Si K-edge. NEXAFS Spectra were baseline corrected and
240 normalized using Athena (Ravel and Newville, 2005). Carbon K-edge peaks were assigned as
241 follows: aromatic C at 285.2 eV, phenolic C at 287.0 eV, aliphatic C at 287.5 eV,
242 carboxylamides at 288.2 eV, carboxylic C at 288.5 eV, and O-alkyl C at 289.4 eV (Kinyangi et
243 al., 2006; Wan et al., 2007; Gillespie et al., 2011; Chen and Sparks, 2015). Principal component

244 analysis of image sequence data was carried out for carbon (Chen and Sparks, 2015). Significant
245 components were identified based on eigenvalues, eigenimages and eigenspectra (Lerotic et al.,
246 2005).

247

248 **2.5. Porewater Sampling**

249 Porewater samples were collected at discrete depths at each vegetation zone using passive
250 porewater samplers (i.e., peepers) in triplicate (i.e., peeper nests) modified from LaForce et al.,
251 (2000). A PVC pipe (21 cm diameter, 152 cm length) housed 9-10 cells, which hold the peepers.
252 Peepers consisted of 13 mL polypropylene tubes fitted with a plastic cap, which contains a 0.20
253 µm nylon membrane and initially filled with 18 MΩ deoxygenated water. The TS zone had
254 peepers at 9 depths (0, -3, -12, -25, -40, -50, -65, -75, -90 cm) and the SS zone had peepers at 10
255 depths (0, -3, -12, -25, -35, -45, -55, -65, -75, -90 cm) relative to the sediment surface as depths
256 were chosen based on sediment profiles with at least two peepers per horizon (Figure S1). The
257 peepers were allowed to equilibrate for at least 10 days (LaForce et al., 2000). After
258 equilibration, the peeper cells were removed from the housing and immediately replaced with
259 fresh peeper cells. When removed from the housing, the peeper cells were immediately placed
260 inside a gas impermeable container with oxygen scrubbers and sealed. The samples were placed
261 on ice and were analyzed or preserved within two hours. Sampling occurred approximately every
262 two weeks between 8/13/14 and 8/24/15, with a three-month hiatus between 12/15/14 to 3/27/15
263 when temperatures were below freezing.

264 During peeper sampling, each water sample was aliquoted into different tubes for various
265 analyses by using a syringe fitted with a needle to pierce the peeper cell membrane and withdraw
266 the 13 mL of equilibrated water sample. Occasionally sediment in the peeper cell was evident

and required filtering with a 0.2 µm nylon syringe filter prior to aliquoting. For redox and pH measurements, a 2 mL sample was placed into a polypropylene tube and measured with calibrated probes within 5 minutes of removing the samples from the sealed, gas-impermeable container. Concurrently, 1 mL of sample was added to a mid-range sulfide determining reagent (8 g N N-dimethyl-*p*-phenylenediamine and 8 g $FeCl_3$ in a 50% HCl solution) and solution was allowed to sit for at least 20 minutes and was then measured at 667 nm in accordance with the Cline method within 24 hours (Cline, 1969). Samples that were out of range were diluted further with deoxygenated water until it was within the range of the spectrophotometer (Reese et al., 2011). Additionally, 0.5 mL of sample was used for Fe(II) analysis using the ferrozine method (Stookey, 1970). Total Fe was obtained using microwave plasma-atomic emission spectrometry (MP-AES, HP 4100) with 5 mL of sample after 1:1 dilution and acidification with 2% trace metal grade nitric acid. At least 1 mL and 3 mL of sample, respectively, were frozen in separate tubes to measure anions via ion chromatography (IC) and dissolved organic carbon (DOC) via TOC analyzer. DOC samples were diluted after thawing in a 1:5 ratio with 18 MΩ water and analyzed (Elementar Vario-TOC cube), and the IC samples were diluted in a 1:3 ratio after thawing. Nitrate, sulfate and phosphate were separated on an AS18 column equipped with an AG18 guard column in gradient elution mode with 20 mM KOH eluent from 0 to 13.5 min and a ramp to 45 mM from 13.5 to 16 minutes and analyzed by IC with electrical conductivity detection (Dionex DX-500). Conductivity was also measured on select samples (Thermofisher Orion STAR A322).

2.6. CO_2 and CH_4 Efflux

289 Measurements of CH_4 and CO_2 efflux were performed using a Los Gatos Research
290 Ultraportable Gas Analyzer (LGR-UGA) using the static chamber method as described in
291 previous studies (Pearson et al., 2016; Warner et al., 2018). Twelve PVC rings (10 cm in
292 diameter) were inserted into the sediment at the TS and SS zones, 6 per zone, and arranged such
293 that they were adjacent to the peeper nests and 180 degrees away from foot traffic in the marsh
294 (Figure 1). No samples were taken until at least 2 weeks after the placement of the rings to allow
295 the area around the rings to recover from the installation. The rings remained in the surface
296 sediments throughout the campaign.

297 During sampling, a PVC static chamber was placed onto the fixed ring, and the chamber
298 was connected to the LGR-UGA with gas-tight tubing for 3 minutes to measure changes in
299 concentrations of CO_2 and CH_4. Field measurements were taken bimonthly between June 2014
300 and September 2015 except for a hiatus during the winter months (12/15/14 to 3/27/15), and
301 were more intensely sampled during the spring thaw in March 2015 (weekly for four weeks).
302 These measurements always occurred within an hour of low tide. Surface sediment temperature
303 was measured concurrently using an infrared thermometer (Arctic Star AR550). Efflux of CO_2
304 and CH_4 (GHG flux) was calculated as previously done (Pearson et al., 2016; Warner et al.,
305 2018) using the following equation:

306 $$GHG\ Flux = \frac{\delta c}{\delta t} * \frac{V}{S} * \frac{P}{RT} \quad (1)$$
307

308 where $\frac{\delta c}{\delta t}$ is the mole fraction of the GHG in μmol mol^{-1} over time (s), V is the volume of the
309 chamber ($0.0011 m^3$), S is the surface area enclosed by the chamber ($0.0081 m^2$), P is the
310 atmospheric pressure (assumed to be 101.325 kPa), R is the universal gas constant ($8.3\times10{-}3$ m^3
311 kPa mol^{-1} K^{-1}), and T is the sediment temperature at time of measurement (K). The change in

concentration of GHG over time, or $\frac{\delta c}{\delta t}$, was calculated by fitting a linear regression for CH_4 and CO_2 throughout each measurement (after discounting 30s as a dead-band). Only values where $r^2 > 0.85$ and $p < 0.05$ were used for flux calculations per standard protocols (Petrakis et al., 2017). All efflux values from SS or from TS zones were averaged together (n=6 per location, Figure 1) for each sampling date.

2.7. CO_2 and CH_4 Depth Profiling

In order to address spatial heterogeneity of GHG production vertically in the sediments, depth profiles of CH_4 and CO_2 concentrations were measured from July 2015 to August 2015 using a passive gas sampling profiler (Figure S2). Gas-permeable silicone tubes (12.7 mm inner diameter and 3.175 mm-thick, (Jacinthe and Groffman, 2001) were placed inside a 2.34 cm x 91.4 cm polypropylene sheet with rectangular through holes cut out at 4 discrete depths relative to the sediment surface based on the horizonation for each zone (Figure S1). One profiler was made for each zone and the depths were -17.5, -30, -50, -68 cm for TS; and -15.5, -40, -56, and -70 cm for SS. Each silicone tube was 23.5 cm long and was attached to gas-tight vinyl tubing on each end by a corrosion-resistant elbow joint. Each joint was made gas- and water-tight with silicone sealant and allowed to dry and harden prior to deployment at the field site. Barbed three-way valves were attached on one end of each of the vinyl tubes and a barbed two-way valve was attached to the other vinyl tube end. Gas-tight Teflon tubing was attached to one of the barbs on the three-way valve for ready coupling to the LGR-UGA with push-to-connect fittings, and Teflon tubing was also attached to the two-way valve barbed for ready coupling to a gas-tight bladder bag of N_2. The apparati were buried at each zone (Figure 1) and allowed to equilibrate with the sediments for two weeks before initial measurements were made. During sampling, the

334 LGR-UGA and N_2 bladder bag were connected to opposite ends, and the valves were opened to
335 allow accumulated gas to flow into the LGR-UGA for measurement. Concentrations of CH_4 and
336 CO_2 were measured until a sharp drop in concentration was observed, indicating the N_2 had
337 cleared the chamber of CH_4 and CO_2. After sampling, the valves were closed to ensure both an
338 air- and water-tight system. This was repeated at each depth at each zone during weekly
339 sampling from 7/13/15-8/12/15. The LGR-UGA's high limit of detection was 892 µM (20,000
340 ppm) for both GHGs, and values over this limit were recorded as >892 µM.
341
342 **2.8. Hydrological Measurements**
343 A monitoring well was placed within 3 m of each peeper nest at each zone (Figure 1).
344 Monitoring wells were constructed of a 152 cm PVC pipe with 91 cm slotted well screen at the
345 bottom of the well (3.12 cm diameter, Atlantic Screen Manufacturing, Inc.). The maximum
346 screened depths for all wells ranged from 99-131 cm with screens extending 91 cm above the
347 bottom of the well. The soil bores were made using a hand auger. The well annulus was filled
348 with sand over the length of the screen and the upper portion filled with mud. A conductivity,
349 temperature, and depth (CTD) sensor (Aqua TROLL 200 Data Logger) was deployed in the well
350 approximately in the middle of the well screen. A pressure transducer (Baro-Diver) was
351 installed at TS to record the atmospheric pressure, and these data were used to calculate water
352 table elevation for both zones according to the following equation:
353

354 $$H = \frac{P_{obs} - P_{Atm}}{\rho g} \quad (2)$$

where P_{obs} is the pressure recorded by the CTD, P_{atm} is the atmospheric pressure, ρ is the water density and g is gravity. The elevation is given relative to marsh surface at each well, determined by measuring the water table depth manually in both wells on 9/22/15. Water table elevations at both wells were measured between 7/8/2015 and 10/6/2015 and covered the range of depths for GHG sampling.

Spring-neap tidal times were determined by using NOAA astronomical data. Where the spring tide time was defined as occurring at full and new moons and neap tides occurring during first and third quarter moons.

2.9. Statistical Analysis

Biogeochemical porewater parameters over time were compared between the two zones by averaging all depths per sampling time and using a two-tailed *t*-test where unequal variance is assumed. Standard error was calculated for each parameter where n=3 for biogeochemical parameters and n=6 for GHG efflux. Variance was calculated across all depths over the entire sampling period for redox values at both zones. GHG efflux from TS and SS were compared using a Mann-Whitney U test with mean-rank comparisons. All analyzes were performed using SPSS version 26.

3. RESULTS

3.1. Sediment Characteristics

Sediments from SS and TS were different and had opposite trends with depth (Table 1). All sediments were acidic but those from SS had pH <3 down to 50 cm depth and increased to 4.3 and 5.7 down to 90 cm. In contrast, sediments from TS were less acidic at the surface with

pH 4.7 and acidity increased with depth with pH ranging 3.3 to 3.6 down to 89 cm depth (Table 1). At SS, percent C increased with depth and ranged 5 to 40%, percent N increased with depth and ranged 0.3 to 1.8%, and percent S was depleted at the 38-50 cm depth (1.3%) and was ~2.5% at all other depths. In contrast, percent C at TS decreased with depth and ranged 8.6 to 14%, and percent N and S were uniform with depth and were ~0.7 and 2%, respectively. TS also had coarser texture than SS likely resulting from coarse-grained sediment depositing on the levee at TS. Extractable Fe phases varied between the two locations, with SS having generally more reducible (i.e., CBD-extractable) Fe and similar poorly-crystalline (i.e., AAO-extractable) Fe, indicating that more Fe reduction may have occurred at TS particularly above 66 cm depth.

Our Fe EXAFS data show that the dominant Fe phases differ among zone locations and with depth (Table 2, Figure S3 and S4). Pyrite is depleted at the 30 cm depth at TS relative to the surface and deeper depths. In contrast, pyrite is depleted in the surface and increases with depth at SS. These trends were also similar for goethite and are the opposite for ferrihydrite. Mackinawite was only present in the surface at SS. Siderite was nearly constant with depth and ~5% of the total in TS, but was lower at SS and decreased with depth to 50 cm before increasing to its highest value of nearly 5% of the total Fe at 70 cm depth (Table 2).

3.2. Porewater

Spatial heterogeneity in porewater chemical signatures was clearly apparent between TS and SS, as well as vertically within each zone (Figure 3 and Figure S5). At both TS and SS, seasonal trends in porewater redox were observed (Figure 3a-b). Redox values across all depths and at both zones decreased during winter plant senescence and then increased during the spring and summer growing season. While both zones showed seasonal variation at all depths, the

401 magnitude of redox values and trends with depth were distinct. The SS zone had significantly
402 lower average redox values compared to TS over time ($p < 0.05$) (Figure 3a-b). Redox values for
403 SS were consistently low and nearly always negative, ranging -200 to 200 mV with depth. In
404 contrast, redox at TS tended to decrease with depth, with the highest redox value of 575 mV
405 recorded at the sediment-air interface and the lowest of -118 mV recorded at depth. This trend
406 was more prevalent during the growing season (May-September). Redox values decreased with
407 depth during the growing season but were more uniform during late fall and winter sampling.
408 The TS zone had an order of magnitude higher variance in redox with depth compared to SS
409 (18581 and 4763, respectively), with average surface porewater redox values ranging widely
410 from 0 to 600 mV, and deeper redox values more narrowly averaged from ca. 0 to 300 mV. The
411 TS zone had more variable pH both with depth and over time compared to SS (Figure S5a-b).
412 The SS location was consistently between a pH of 6 and 7, whereas TS had variation near the
413 surface, ranging from 3.5 to 7.6.

414 The TS zone has more variable DOC both with depth and over time compared to SS
415 (Figure 3c-d). Concentrations ranged from non-detectable to 8 mM at TS. In contrast, SS
416 exhibited little variation in DOC concentration with both depth and time with values ranging
417 from non-detectable to 2 mM.

418 The TS and SS zones differed greatly in the magnitude and speciation of Fe and S
419 compounds in porewater (Figure 3e-h and Figure S5c-f). Total Fe at TS was as high as 1.5 mM
420 and increased with depth (Figure S5e) whereas total Fe at SS was rarely detectable (Figure S5f)
421 despite similar amounts of CBD- and AAO-extractable iron (Table 1). Similar trends were
422 observed with Fe(II), with concentrations up to 1.0 mM at TS and almost always non-detectable

423 at SS (Figure 3e-f). At TS, total Fe concentrations equaled Fe (II) concentrations at depth
424 indicating that all the iron present was reduced at depth below -12 cm.
425 In contrast to Fe, concentrations of S compounds at SS were higher than at TS. Sulfide
426 concentrations were non-detectable at TS (Figure 3g) but were detectable at all depths at SS
427 ranging 0.10 to 2.2 mM and tending to increase with depth (Figure 3h). Sulfate concentrations
428 varied with depth throughout the year, and ranged from non-detectable to 9.0 mM at TS but
429 ranged 3.0 to 18 mM at SS (Figure S5c-d).

430 **3.3. CO_2 and CH_4 Efflux**

431 Differences in the ranges and daily average of CO_2 and CH_4 were observed between the
432 two locations (Figure 4). At TS, CH_4 efflux ranged from -0.0002 to as high as 3.04 μmol m^{-2} s^{-1}
433 with an average daily efflux of 9.4 (± 20) mmol m^{-2} d^{-1}, and CO_2 efflux ranged from -0.5 to as
434 high as 42.2 μmol m^{-2} s^{-1} with an average daily efflux of 469 (± 538) mmol m^{-2} d^{-1}. At SS, CH_4
435 efflux ranged from 0 to as high as 2.5 μmol m^{-2} s^{-1} with an average daily efflux of 12.2 (± 29)
436 mmol m^{-2} d^{-1}, and CO_2 efflux ranged from -0.9 to as high as 22 μmol m^{-2} s^{-1} with an average
437 daily efflux of 208 (± 248) mmol m^{-2} d^{-1}.
438 There were distinct seasonal trends in efflux of both CH_4 and CO_2 at both locations
439 (Figure 4). The highest efflux of CH_4 and CO_2 at both locations was observed during the middle
440 of the summer growing seasons and declined to near zero during plant senescence in the late fall
441 and winter (Figure 4). Efflux of CO_2 was consistently higher for TS compared to SS, whereas the
442 pattern for CH_4 was less clear. Efflux of CH_4 spiked in July-September at both locations for both
443 years, yet the magnitude differed for each year with SS having a higher CH_4 spike (up to ~2.5
444 μmol m^{-2} s^{-1}) than TS in 2014, and the converse was observed in 2015 (Figure 4a). A Mann-
445 Whitney U test revealed that efflux of CO_2 was statistically significantly higher at TS (U = 2876,

446 $p < 0.0001$), whereas efflux of CH_4 was statistically significantly higher at SS ($U = 2173$, $p =$
447 0.002) over the study period.
448
449 **3.4. Water Table Elevations and CO_2 and CH_4 Production with Depth**
450 We observed large differences in water table elevations, oscillations, and periods of land
451 surface inundation between the two zones (Figure 5a). The TS and SS locations had significantly
452 different water levels ($p < 0.05$) over the measured time period of 8 July 2015- 12 August 2015.
453 The SS location exhibited daily tidal variations in water level, whereas TS exhibited both daily
454 tidal variation in water level as well as larger variation over longer time scales associated with
455 the spring-neap cycle (Figure 5a). The water level at SS ranged from ca. -5 cm to as high as +18
456 cm relative to the marsh surface, and sediments were usually completely saturated. In contrast,
457 water level at TS ranged from -25 cm to +10 cm with distinct periods of unsaturation down to -
458 25 cm depth (Figure 5a).
459 Depth profiles of CO_2 and CH_4 concentrations taken on 5 different days over the spring-
460 neap tidal cycle show an apparent build-up of both CH_4 and CO_2 concentrations in the
461 subsurface at both zones that varied in location and magnitude and at times reached the upper
462 limit of detection (892 μM) of the instrument (Figure 5b-e). At TS, CH_4 concentrations were low
463 (< 100 μM) at the near-surface sampling depths and increased with depth to at least 892 μM
464 (Fig. 5b). As the water table elevation decreased from nearly 0 to -25 cm (Figure 5a), CH_4
465 concentrations at depths >50 cm increased from <100 to at least 892 μM and decreased again to
466 300 – 600 μM as the water table elevation fluctuated (Figure 5a-b). In contrast, CO_2
467 concentrations at TS were higher than for CH_4 and ranged from 209 to >892 μM. For almost all

468 sampling dates, CO_2 concentration was at least 892 μM at -30 cm and below except for one
469 sampling point shown in orange at -50 cm depth at TS (Figure 5c).
470 Both the CH_4 and CO_2 depth profiles at SS differed from TS (Figure 5b-e). During times
471 of prolonged inundation at SS, CH_4 concentrations were high in the near-surface depths (within -
472 20 cm) and ranged ca. 300 to 700 μM (Figure 5a and d, red and blue). In contrast, during times
473 of water table draw down, CH_4 concentrations at SS were non-detectable within -20 cm (Figure
474 5a and d, orange and yellow). Despite differences in near-surface concentrations, CH_4 levels
475 increased with depths of -40 cm and below regardless of the tidal cycle and ranged ca. 300 to at
476 least 892 μM (Figure 5d). The CO_2 concentrations at SS tended to be lower than at TS for the
477 near-surface depths, but they were similar between zones below -40 cm depth (Figure 5c and e).
478
479 **3.5. STXM-NEXAFS**
480 To better understand the C-mineral associations of the bulk sediments as potential factors
481 that contributed to differences in C dynamics between zones, we examined sediment chemistry at
482 50 and 56 cm depth with STXM-NEXAFS. Principal component analyses (PCA) of the STXM-
483 NEXAFS data revealed three components for each sample, but these components differed among
484 zones (Figure 6 and S6-7). In TS there were three components, but each had relatively uniform C
485 speciation with predominant C K-edge NEXAFS peaks indicating the presence of aromatic and
486 carboxylic C in all components (Figure 6 and S6). In contrast, the PCA of the sediment sample
487 from SS revealed three components that differed greatly in chemical composition with three
488 distinct regions: C associated with biological material, quartz with no detectable C, and non-
489 quartz sediment grains (Figure 6 and S7). The SS vegetation zone showed the presence of
490 aromatic C and carboxylic C, though with more pronounced shoulders in the phenolic and

aliphatic region than in TS (Figure 6). In particular, the biological material in SS displayed the strongest aromatic peak and the highest intensity in the phenolic and aliphatic region. Correlation analyses (Figure S8) of the optical densities (ODs) for each element examined indicated that Ca had the strongest spatial association with C ($R^2 = 0.232$, $p<0.0001$) compared with any other element analyzed in SS. In contrast, Fe displayed the strongest correlation with C ($R^2 = 0.284$, $p<0.0001$) in TS.

4. DISCUSSION

Our data show that water table depth variability results in both a lateral (across the marsh) and vertical (with depth) heterogeneity in biogeochemical processes that, in turn, results in a large spatial heterogeneity of CO_2 and CH_4 production and efflux. We hypothesized that 1) vegetation zones near the tidal channel will have a greater change in water table elevation resulting in more oxidizing sediments than zones farther from the tidal channel, and 2) zones with greater change in water table elevation will have a higher rate of CO_2 and CH_4 efflux than those zones with less variation in water table elevation. Our data support both hypotheses, and we observed differences in mineral control on stored C and a pool of stored C as CO_2 and CH_4 below ~40 cm depth in sulfate-rich (up to 17 mM) porewaters. The observed CH_4 of at least 892 µM was an order of magnitude higher than reported in sulfate-rich sediments and on par with or up to 2 fold higher than those reported in freshwater systems and in marine systems below the sulfate-methane transition zone (Martens and Berner, 1977; Kelley et al., 1995; Angle et al., 2017; Xiao et al., 2018). Because these stored C-based greenhouse gases were dynamic and varied across the landscape, our results may help explain the wide ranges of C fluxes from salt

513 marsh ecosystems, which has implications for potential land use change, weather variability and
514 future environmental change.
515
516 **4.1. Spatial heterogeneity in biogeochemical processes between zones**
517 The landscape of the Mid-Atlantic tidal salt marsh under study in this work was similar to
518 those described previously in Georgia having high tidal amplitudes (Nestler, 1977a; Wiegert and
519 Freeman, 1990), which led to differences in dominant biogeochemical processes of interstitial
520 waters across zones. The high tidal amplitude of ~2 m (Figure 1b) led to the formation of a
521 natural levee near the creek bank, which drove differences in redox status of interstitial waters in
522 SS in the marsh interior and TS near the tidal channel. As described by Nestler (1977a), the
523 natural levee near the creek bank forms as the incoming tide deposits its sediment load. This
524 levee limits the creek water from reaching SS except in extreme high tides where creek water can
525 overtop the levee. Therefore, the interstitial water in SS does not readily exchange with creek
526 waters and can become strongly anaerobic (Nestler, 1977b; Nestler, 1977a). The SS zone had
527 lower DOC concentrations that were relatively uniform with depth. This suggests little exchange
528 with creek water, which brings in DOC with the incoming tides (Hemminga et al., 1992;
529 Hemminga et al., 1993). We also observed strongly reducing interstitial water in SS where redox
530 potentials were less than 100 mV down to ~ 1 m depth throughout the seasons and sulfide
531 concentrations were as high as 2 mM (Figure 3a and h). While we did not observe Fe(II) in
532 interstitial waters (Figure 3f), the increase in pyrite in the sediment solid phase (Table 2)
533 suggests that as ferric oxides were reduced concurrently with sulfate (Postma and Jakobsen,
534 1996), ferrous sulfide minerals formed that sequestered Fe(II) from solution (Howarth et al.,

1984; Morse et al., 1987). While SS experienced tidal oscillations, the water table elevation was always near the sediment surface (Figure 5a), further enhancing strongly anaerobic sediments.

In contrast to SS, the sediments of TS were more strongly oxidizing due to relatively higher elevation of the natural levee and proximity to the tidal creek, which led to more unsaturated sediments during ebb tides particularly over spring-neap cycles. These spring-neap cycles lowered the water table level to as much as -25 cm relative to the sediment surface at TS, which provided conduits for gas exchange. Together with more exposed sediments due to higher elevation, the sediments at TS were more oxidizing than at SS (Figure 5a). The TS location experienced more variable and higher redox potentials that never reached sulfate-reducing conditions down to ~ 1 m depth, and there was no detectable sulfide in interstitial porewaters despite up to 8 mM sulfate (Figure 3g and Figure S5c). Instead, these porewaters contained ferrous iron that tended to increase in concentration with depth, ranging from non-detectable at the surface to ca. 0.8 mM. The lack of ferrous iron at the surface was most likely because of the outgoing tide dropping the water table elevation to below the first few surface peeper cells, which likely caused any ferrous iron in those samples to oxidize between sampling events.

Because we observed different dominant geochemistry with depth > 40 cm at both zones and an order of magnitude higher %C at SS at that depth (Table 1), we explored the C chemistry of the sediment solid phase below this threshold to explore controls on C-stabilization in sediments. STXM-NEXAFS analysis revealed that the C at > 40 cm depth at TS was uniformly distributed and consisted of carboxyl and carboxylamide groups, indicative of degraded C (Kinyangi et al., 2006) and was most associated with Fe. This could indicate organic matter coatings on Fe-bearing minerals that were dynamic with redox oscillations at TS (Chen et al., 2018). Fe-mineral associations with organic matter have been observed in a wide variety of soil

environments and tend to dominate at acidic pH (Mikutta et al., 2006; Rasmussen et al., 2006; Wagai and Mayer, 2007; Rowley et al., 2018; Rasmussen et al., 2018; Chen et al., 2018; LaCroix et al., 2019), but there has been limited data in wetland ecosystems. A recent meta-analysis that suggests pH as the master variable for predicting SOC stocks excluded histosols and organic horizons from the analysis (Rasmussen et al., 2018). The data presented here appear to fit the model that low pH and the presence of Fe oxides exert at least partial control on C retention in near-channel marsh sediments, but likely redox exerts a stronger control (LaCroix et al., 2019).

In contrast to TS, the accumulated C at > 40 cm depth at SS was heterogeneously distributed. While a cluster of this C was similar to TS showing degraded carbon with Fe association (Figure 6, yellow cluster), another cluster of this C showed strong aromatic and phenolic C signature (Figure 6, green cluster), which is indicative of plant-derived material (Figure 6). The plant signature of this C suggests that some of the C at depth at SS is physically protected from degradation likely due mainly to reducing conditions that limit aerobic C oxidation (Rowley et al., 2018; LaCroix et al., 2019). In addition, the C at SS in the entire sample was correlated best with Ca, and particularly for the plant-derived C (Figure 6 and Figure S7); a strong Ca-C association has been observed previously in a sample from a freshwater wetland (Chen and Sparks, 2015). It is noteworthy that the Ca-C association in our study occurred in acidic sediments (pH = 4.3), which is in contrast to the general view that Ca-C control dominates at basic pH (Rowley et al., 2018; Rasmussen et al., 2018). Our findings could simply indicate that the >30% C at that depth held more Ca on exchange sites (Table 1), or it could also suggest that the cluster contains protected carbon from plant cell walls, as Ca^{2+} is well-known to bind onto the negatively-charged cell walls and provide structural stability to cell walls and membranes (Marschner, 2003). However, a partial Ca control on C stability via cation bridging

581 by inner sphere or outer sphere complexes may also be at play (Rowley et al., 2018), particularly
582 as these sediments had little evidence of Fe cycling. We highlight that this is an important
583 knowledge gab and more research is needed in order to unravel these potential Ca-C associations
584 in saline, wetland sediments.
585
586 **4.2 Seasonal dynamics of GHG fluxes between zones**
587 As we hypothesized, TS had significantly higher efflux of CO_2 but not CH_4 than SS over
588 the sampling period. While efflux of CH_4 was generally similar for TS and SS, one sampling
589 event in summer resulted in a pulse of CH_4 at SS likely driven by ebullition, which resulted in
590 statistically higher efflux of CH_4 at SS over the sampling period (Figure 4). Similar to our study,
591 King and Wiebe (1978) also observed that CH_4 efflux from a SS location in a Georgia salt marsh
592 was predominantly from ebullition events. The higher magnitude of C efflux from TS is likely
593 due to escape of trapped gases as the water table elevation dropped to as low as -25 cm and
594 enhanced heterotrophic activity associated with higher DOC. While we did not directly measure
595 heterotrophic activity, the nearly 3-fold higher %C in surface sediments and higher porewater
596 DOC of TS implies more available substrate supply for maintaining microbial biomass and
597 activity within these sediments (Table 1). In addition, there was likely more CO_2 produced in
598 sediments at TS than at SS due to more energetically favorable metabolisms in the less reducing
599 sediments of TS. Like King and Wiebe (1978), we also observed higher C efflux during
600 summers. This is likely due to both enhanced DOC due to plant activity and warmer
601 temperatures as expected in a typical temperature dependence for CO_2 production and efflux
602 (Alperin et al., 1994; Fang and Moncrieff, 2001).
603

604 **4.3. Pathways and Fate of CO_2 and CH_4 production in sediments**

605 Because we observed highest fluxes of CO_2 and CH_4 in summer, we took a closer look at
606 production of these gases between July-August 2015. These results revealed a large pool of
607 stored CO_2 and CH_4 with depth > -25 cm that differed in magnitude between zones. Despite
608 higher redox potentials favoring iron reduction at depths down to ~1 m at TS, these sediments
609 below 40 cm depth contained 75 to >892 µM CH_4, the upper limit of detection of the LGR
610 instrument used. Higher porewater CH_4 was observed at SS that ranged 250 to >892 µM CH_4.
611 These values are higher than values previously reported from three sites along a tidal creek of a
612 salt marsh near the Chesapeake Bay where values <500 µM CH_4 down to 60 cm depth were
613 reported (Bartlett et al., 1987). Our observed values are also 2 orders of magnitude higher than
614 CH_4 concentrations in sediments of a tidal lagoon (Deborde et al., 2010). Our depth profiles of
615 CH_4 are more similar to those reported for freshwater wetlands or for those reported in marine
616 sediments below the sulfate-methane transition zone. Angle et al. (2017) reported dissolved CH_4
617 of up to ~400 µM in sediments down to 35 cm depth in a freshwater wetland off of the Lake Erie
618 shore, and Kelley et al. (1995) observed dissolved CH_4 as high as 900 µM using peepers and GC
619 detection in a tidal freshwater marsh in North Carolina. Note that in our study, the concentrations
620 of CH_4 at depth may be even higher than 892 µM, but a different instrument with a higher range
621 of detection would need to be used, as the LGR-UGA is designed for accurate detection of trace
622 gas concentrations. The high values of CH_4 at depth at TS occurred when SO_4^{2-} concentrations
623 were only has high as 6 mM, but those at SS occurred at SO_4^{2-} as high as 17 mM, which suggests
624 differences in the pathway of methane production across the marsh platform.

625 Our data suggest that CH_4 was being produced at depth in both zones by different
626 pathways, but CH_4 was either not produced at the surface when the water level elevation dropped

627 below the sediment surface, it was consumed by methanotrophic microorganisms thriving in the
628 surface sediments (Conrad, 2007; Trotsenko and Murrell, 2008; Knittel and Boetius, 2009;
629 Ettwig et al., 2010; Penido et al., 2016; Ettwig et al., 2016), or it was effluxed to the atmosphere.
630 The TS zone along the creek bank is a classic example of redox zonation where more oxidizing
631 sediments at the surface transitioned to more reducing sediments are at depth, which supported
632 iron reduction near the surface and CH_4 production at depth. The relatively low SO_4^{2-}
633 concentrations (non-detect to 6 mM) and non-detectable sulfide at depth at TS indicates that CH_4
634 production there could have proceeded via hydrogenotrophic or aceticlastic pathways as sulfate
635 reducing bacteria were likely not competing with methanogens for substrate. This helps to
636 explain why CH_4 concentrations at depth at TS were similar to those reported for freshwater
637 wetlands (Kelley et al., 1995; Angle et al., 2017). In surface sediments <20 cm depth, TS
638 porewaters contained nearly non-detectable CH_4, which suggests that CH_4 produced at depth and
639 diffusing upward could have been partially consumed by methanotrophs either via aerobic or
640 anaerobic metabolisms (Trotsenko and Murrell, 2008; Knittel and Boetius, 2009). The evidence
641 of Fe reduction in sub-oxic TS sediments and relatively high proportion of ferrihydrite suggests
642 that CH_4 consumption could have proceeded via anaerobic methanotrophic archaea who use
643 Fe(III) from nanoparticulate ferrihydrite an electron acceptor (Ettwig et al., 2016). Any CH_4 that
644 was not consumed by methanotrophs could have been rapidly effluxed to the atmosphere when
645 the water table oscillated as low as -25cm.
646 In contrast to TS near the tidal channel, CH_4 production at SS in the marsh interior likely
647 proceeded via methylotrophic methanogenesis at depth, and this CH_4 had likely slower rates of
648 methanotrophic consumption due to more strongly reducing conditions in surface sediments. The
649 relatively high porewater CH_4 at depths below 40 cm coincided with up to 17 mM SO_4^{2-} and 2 –

650 3 mM S^{2-}. Because sulfate reduction was occurring with methanogenesis, this suggests that
651 methylotrophic methanogensis, where sulfate reducing bacteria do not compete for substrate,
652 was the dominate pathway at SS, and the responsible microorganisms were active at depths as
653 low as -70 cm relative to the sediment surface. This depth is deeper than previously reported for
654 marine sediments where methylotrophic methanogenesis dominated in surface sediments (0 – 10
655 cm) when SO_4^{2-} was near 25 mM and transitioned to aceticlastic methanogenesis below the
656 sulfate-methane transition zone as SO_4^{2-} approached non-detectable levels (Xiao et al., 2017;
657 Xiao et al., 2018). The high rate of biomass burial of decaying of *S. alterniflora* tissues, which
658 release methylamine compounds (Wang and Lee, 1994), likely contributed to the deeper extent
659 of methylotrophic CH_4 production than in marine sediments; methylamines are known to be
660 higher in salt marshes than in marine sediments (Fitzsimons et al., 1997). The higher porewater
661 CH_4 at SS in the surface (0 – 40 cm) at SS than TS was likely because there was less
662 energetically favorable methanotrophy (e.g., sulfate-mediated anaerobic methanotrophy)
663 occurring in these more reducing sediments compared to TS.
664 Similar to CH_4, dissolved CO_2 concentrations were elevated with depth >40 cm for
665 almost all sampling events in both zones and were variable but typically lower at the surface <40
666 cm, particularly for TS. The only CO_2 concentration at depth that was less than detector
667 saturation (892 μM) occurred at TS during the lowest low tide under study (Figure 5a and c), and
668 the only surface CO_2 concentration that was >892 μM occurred at the highest high tides under
669 study. This suggests that CO_2 produced at depth is stored within the sediment column with
670 limited routes for vertical diffusion due to low diffusivity when sediments are saturated, but can
671 be flushed out during extreme low tide events nearest the tidal channels when diffusivity rates

672 increase. Thus, the fluxes of GHGs in this ecosystem can vary in space and time due to a
673 combination of biogeochemical and hydrological drivers.

674 The high concentrations of CO_2 and CH_4 at depths down to ~ 1 m in our study
675 demonstrate the existence of an unquantified pool of porewater CH_4 and CO_2 in sediments of salt
676 marshes. We computed median values of CO_2 and CH_4 at both TS and SS zones, and while they
677 were equivalent across zones for CO_2 (892 µM), they were 20x higher at the SS zone for CH_4
678 (74 µM for TS and 634 µM for SS). While our data are limited to summer measurements in one
679 marsh and may not reflect global temperate marshes, it is useful to consider the global context of
680 these findings. Assuming an extent of 5.3 Mha of temperate salt marshes worldwide (Pendleton
681 et al., 2012; Mcowen et al., 2017), the relative distribution of zone area in our marsh of TS
682 (37%) and SS (63%), an estimated 1:1 solid:water ratio of the sediments, and an estimated 0.9 g
683 cm^{-3} bulk density, we computed a conservative estimate of ~70 Gg C in salt marsh porewater to
684 1 m depth. Of this, ~21 Gg C is as CH_4 in SS zones and only <2 Gg C is as CH_4 in TS zones.
685 Because most research tends to focus on areas near the tidal channel or creek bank, the high CH_4
686 in sulfate-rich SS zones may have been overlooked in past studies.

687 It is often assumed that salt marshes have a high potential for C sequestration due to
688 sulfate reduction limiting the rates of methanogenesis (Chmura et al., 2003; Mcleod et al., 2011),
689 but our data suggest that methylotrophic methanogenesis is responsible for high CH_4 levels in SS
690 zones of salt marshes, which according to our calculations make up at least 60% of marsh area.
691 Supporting this is recent work in Jiangsu, China where S. *alterniflora* invasion has resulted in
692 higher CH_4 efflux as the microbial community shifts from hydrogenotrophic to methylotrophic
693 methanogenesis (Yuan et al., 2019) due to release of methylamines from decaying S. *alterniflora*
694 biomass (Wang and Lee, 1994). Importantly, this stored pool of CH_4 could be rapidly lost to the

atmosphere by land use change. For example, drainage of a salt marsh will result in rapid changes of physical properties (e.g., decrease of pore water), will suddenly increase GHG diffusion rates and will result in abrupt loss of stored CH_4 and CO_2 to the atmosphere. This C pool and sensitive immediate potential loss after land use change is currently not accounted for in local-to-global wetland C inventories (Petrescu et al., 2015; Hayes et al., 2018).

5. CONCLUSIONS

By coupling geochemical, biophysical and hydrologic measurements, this study revealed different drivers and controls on C cycling depending on location in a tidal salt marsh. Despite their small area of the Earth's crust, tidal salt marshes store disproportionately high amounts of C in sediments, 1-3 orders of magnitude higher than forests and other wetland ecosystems. This stored carbon has largely been thought of as resistant to degradation and therefore stable due to low rates of carbon oxidation under reducing conditions. Our data partially support this paradigm as we observed C accumulation at depth >50 cm in sediments of salt marsh interiors, but not in sediments near tidal channels. Moreover, our data reveal at least partial mineral control of C at depth via C-Fe interactions in sediments near tidal channels, but perhaps C-Ca interactions in salt marsh interiors, but these relationships must be further explored.

Salt marshes are also assumed to have limited CH_4 production due to competition between sulfate reducing bacteria and methanogens for substrate. However, our data show that CH_4 production coincides with sulfate reduction and appears to proceed via methylotrophic methanogenesis pathway in which sulfate-reducing bacteria do not compete for substrate. Therefore, while efflux appears to be low, it should not be assumed that these ecosystems do not produce CH_4. We observed concentrations of CH_4 at depth that were higher than those observed

718 in freshwater wetlands and marine sediments. This sediment C is prone to be lost to the
719 atmosphere with disturbance or land-use change.

720 Modeling efforts that are ongoing to predict future changes to C dynamics in these
721 systems should consider the spatial heterogeneity that exists across the landscape and with depth
722 in these sensitive ecosystems. Future work should focus on refining predictive models to capture
723 differences in C across marsh vegetation zones and on coupling measurements of C age with
724 microbial activity to reveal the drivers for stored C at depth. Moreover, future research across
725 wetlands should include (bio)geochemical information to explain spatial and temporal dynamics
726 of GHG fluxes for future incorporation of these processes in Earth System Models (Phillips et
727 al., 2017).

728

729 **Acknowledgements**

730 We thank the St. Jones National Estuarine Reserve staff for access to the research site and
731 Sandra Petrakis, Erica Loudermilk, Andrew Morris, Jessica Mann and Nicholas Kaufman for
732 help with data collection. This project was funded by the University of Delaware College of
733 Agriculture and Natural Resources Competitive Seed Grant Program (R.V. and A.L.S.), NOAA-
734 DNREC (R.V. and A.L.S.), the National Science Foundation Grant No. 1759879 (H.M. and
735 A.L.S.) and 1652594 (R.V.), the Delaware Environmental Institute (J.W.S., K.K.), and the
736 Delaware Water Resources Program (K.K.) STXM analyses were performed at the SM beamline
737 of the Canadian Light Source, which is supported by the Natural Sciences and Engineering
738 Research Council of Canada, the National Research Council of Canada, the Canadian Institutes
739 of Health Research, the Province of Saskatchewan, Western Economic Diversification Canada,

740 and the University of Saskatchewan. Fe EXAFS and XRD analyses were performed at the
741 Stanford Synchrotron Radiation Lightsource, SLAC National Accelerator Laboratory, which is
742 supported by the U.S. Department of Energy, Office of Science, Office of Basic Energy Sciences
743 under Contract No. DE-AC02-76SF00515.

744

745 **References**

746 Alperin M. J., Albert D. B. and Martens C. S. (1994) Seasonal variations in production and
747 consumption rates of dissolved organic carbon in an organic-rich coastal sediment.
748 *Geochim. Cosmochim. Acta* **58**, 4909–4930.

749 Angle J. C., Morin T. H., Solden L. M., Narrowe A. B., Smith G. J., Borton M. A., Rey-Sanchez
750 C., Daly R. A., Mirfenderesgi G., Hoyt D. W., Riley W. J., Miller C. S., Bohrer G. and
751 Wrighton K. C. (2017) Methanogenesis in oxygenated soils is a substantial fraction of
752 wetland methane emissions. *Nat. Commun.* **8**.

753 Bartlett K. B., Bartlett D. S., Harriss R. C., Sebacher D. I. and Robert C. (1987) Methane
754 emissions along a salt marsh salinity gradient. *Biogeochemistry* **4**, 183–202.

755 Bartlett K. B., Harriss R. C. and Sebacher D. I. (1985) Methane flux from coastal salt marshes. *J.*
756 *Geophys. Res.* **90**, 5710–5720.

757 Beck M., Dellwig O., Liebezeit G., Schnetger B. and Brumsack H. J. (2008) Spatial and seasonal
758 variations of sulphate, dissolved organic carbon, and nutrients in deep pore waters of
759 intertidal flat sediments. *Estuar. Coast. Shelf Sci.* **79**, 307–316.

760 Bethke C. M., Sanford R. A., Kirk M. F., Jin Q. S. and Flynn T. M. (2011) The thermodynamic

761 ladder in geomicrobiology. *Am. J. Sci.* **311**, 183–210.

762 Call M., Maher D. T., Santos I. R., Ruiz-Halpern S., Mangion P., Sanders C. J., Erler D. V.,
763 Oakes J. M., Rosentreter J., Murray R. and Eyre B. D. (2015) Spatial and temporal
764 variability of carbon dioxide and methane fluxes over semi-diurnal and spring–neap–spring
765 timescales in a mangrove creek. *Geochim. Cosmochim. Acta* **150**, 211–225.

766 Cao L., Zhou Z., Xu X. and Shi F. (2020) Spatial and temporal variations of the greenhouse gas
767 emissions in coastal saline wetlands in southeastern China. *Environ. Sci. Pollut. Res.* **27**,
768 1118–1130.

769 Capooci M., Barba J., Seyfferth A. L. and Vargas R. (2019) Experimental influence of storm-
770 surge salinity on soil greenhouse gas emissions from a tidal salt marsh. *Sci. Total Environ.*
771 **686**, 1164–1172. Available at:
772 http://www.sciencedirect.com/science/article/pii/S0048969719325860.

773 Chanton J. P., Martens C. S. and Kelley C. a. (1989) Gas transport from methane-saturated, tidal
774 freshwater and wetland sediments. *Limnol. Oceanogr.* **34**, 807–819.

775 Chen C., Dynes J., Wang J., Karunakaran C. and Sparks D. L. (2014) Soft X-ray
776 Spectromicroscopy Study of Mineral-Organic Matter Associations in Pasture Soil Clay
777 Fractions. *Environ. Sci. Technol.* **48**, 6678–6686.

778 Chen C., Meile C., Wilmoth J., Barcellos D. and Thompson A. (2018) Influence of pO(2) on Iron
779 Redox Cycling and Anaerobic Organic Carbon Mineralization in a Humid Tropical Forest
780 Soil. *Environ. Sci. Technol.* **52**, 7709–7719.

781 Chen C. and Sparks D. L. (2015) Multi-elemental scanning transmission X-ray microscopy–near

782 edge X-ray absorption fine structure spectroscopy assessment of organo–mineral
783 associations in soils from reduced environments. *Environ. Chem.* **12**, 64–73.

784 Chmura G. L., Anisfeld S. C., Cahoon D. R. and Lynch J. C. (2003) Global carbon sequestration
785 in tidal, saline wetland soils. *Global Biogeochem. Cycles* **17**.

786 Cline J. (1969) Spectrophotometric determination of hydrogen sulfide in natural waters. *Limnol.*
787 *Oceanogr.* **14**, 454–458.

788 Conrad R. (2007) Microbial Ecology of Methanogens and Methanotrophs. In *Advances in*
789 *Agronomy* (ed. Sparks, DL). Advances in Agronomy. ELSEVIER ACADEMIC PRESS
790 INC, 525 B STREET, SUITE 1900, SAN DIEGO, CA 92101-4495 USA. pp. 1–63.

791 Darling W. G. and Gooddy D. C. (2006) The hydrogeochemistry of methane: Evidence from
792 English groundwaters. *Chem. Geol.* **229**, 293–312.

793 Deborde J., Anschutz P., Guerin F., Poirier D., Marty D., Boucher G., Thouzeau G., Canton M.
794 and Abril G. (2010) Methane sources, sinks and fluxes in a temperate tidal Lagoon: The
795 Arcachon lagoon (SW France). *Estuar. Coast. Shelf Sci.* **89**, 256–266.

796 Drabsch J. M., Parnell K. E., Hume T. M. and Dolphin T. J. (1999) The capillary fringe and the
797 water table in an intertidal estuarine sand flat. *Estuar. Coast. Shelf Sci.* **48**, 215–222.

798 Dynes J. J., Regier T. Z., Snape I., Siciliano S. D. and Peak D. (2015) Validating the Scalability
799 of Soft X-ray Spectromicroscopy for Quantitative Soil Ecology and Biogeochemistry
800 Research. *Environ. Sci. Technol.* **49**, 1035–1042.

801 Ettwig K. F., Butler M. K., Le Paslier D., Pelletier E., Mangenot S., Kuypers M. M. M.,
802 Schreiber F., Dutilh B. E., Zedelius J., de Beer D., Gloerich J., Wessels H. J. C. T., van

803 Alen T., Luesken F., Wu M. L., van de Pas-Schoonen K. T., den Camp H. J. M. O.,
804 Janssen-Megens E. M., Francoijs K.-J., Stunnenberg H., Weissenbach J., Jetten M. S. M.
805 and Strous M. (2010) Nitrite-driven anaerobic methane oxidation by oxygenic bacteria.
806 *Nature* **464**, 543+.

807 Ettwig K. F., Zhu B., Speth D., Keltjens J. T., Jetten M. S. M. and Kartal B. (2016) Archaea
808 catalyze iron-dependent anaerobic oxidation of methane. *Proc. Natl. Acad. Sci. U. S. A.* **113**,
809 12792–12796.

810 Fagherazzi S., Wiberg P. L., Temmerman S., Struyf E., Zhao Y. and Raymond P. a (2013)
811 Fluxes of water, sediments, and biogeochemical compounds in salt marshes. *Ecol. Process.*
812 **2**, 3.

813 Fang C. and Moncrieff J. B. (2001) The dependence of soil CO2 efflux on temperature. *Soil Biol.*
814 *Biochem.* **33**, 155–165.

815 Fitzsimons M. F., Jemmett A. W. and Wolff G. A. (1997) A preliminary study of the
816 geochemistry of methylamines in a salt marsh. *Org. Geochem.* **27**, 15–24.

817 Gillespie A. W., Walley F. L., Farrell R. E., Leinweber P., Eckhardt K.-U., Regier T. Z. and
818 Blyth R. I. R. (2011) XANES and pyrolysis-FIMS evidence of organic matter composition
819 in a hummocky landscape. *Soil Sci. Soc. Am. J.* **75**, 1741–1755.

820 Grunwald M., Dellwig O., Beck M., Dippner J. W., Freund J. a., Kohlmeier C., Schnetger B. and
821 Brumsack H. J. (2009) Methane in the southern North Sea: Sources, spatial distribution and
822 budgets. *Estuar. Coast. Shelf Sci.* **81**, 445–456.

823 Hansel C. M., Benner S. G., Neiss J., Dohnalkova A., Kukkadapu R. K. and Fendorf S. (2003)

824 Secondary mineralization pathways induced by dissimilatory iron reduction of ferrihydrite
825 under advective flow. *Geochim. Cosmochim. Acta* **67**, 2977–2992.

826 Hayes D. J., Vargas R., Alin S. R., Conant R. T., Hutyra L. R., Jacobson A. R., Kurz W. A., Liu
827 S., McGuire A. D., Poulter B. and Woodall C. W. (2018) *Chapter 2: The North American*
828 *carbon budget*. eds. N. Cavallaro, G. Shrestha, R. Birdsey, M. A. Mayes, R. G. Najjar, S. C.
829 Reed, P. Romero-Lankao, and Z. Zhu, U.S. Global Change Research Program, Washington,
830 D.C.

831 Hemminga M. A., Klap V. A., Van Soelen J. and Boon J. J. (1993) Effect of salt marsh
832 inundation on estuarine particulate organic matter characteristics. *Mar. Ecol. Prog. Ser.* **99**,
833 153–161.

834 Hemminga M. A., Klap V. A., van Soelen J., de Leeuw J. and Boon J. J. (1992) Shifts in seston
835 characteristics after inundation of a European coastal salt marsh. *Limnol. Oceanogr.* **37**,
836 1559–1564.

837 Hippe H., Caspari D., Fiebig K. and Gottschalk G. (1979) Utilization of trimethylamine and
838 other N methyl compounds for growth and methane formation by Methanosarcina barkeri.
839 *Proc. Natl. Acad. Sci. U. S. A.* **76**, 494–498.

840 Holmer M. and Kristensen E. (1994) Coexistence of sulfate reduction and methane production in
841 an organic-rich sediment. *Mar. Ecol. Prog. Ser.* **107**, 177–184.

842 Howarth R. W., Merkel S. and May N. (1984) Pyrite Formation and the Measurement in Salt
843 Marsh Sediments. **29**, 598–608.

844 IPCC (2014) *Climate Change 2014: mitigation of climate change*., Cambridge University Press,

845 New York, NY.

846 Jacinthe P. A. and Groffman P. M. (2001) Silicone rubber sampler to measure dissolved gases in
847 saturated soils and waters. *Soil Biol. Biochem.* **33**, 907–912.

848 Jones H. J., Kroeber E., Stephenson J., Mausz M. A., Jameson E., Millard A., Purdy K. J. and
849 Chen Y. (2019) A new family of uncultivated bacteria involved in methanogenesis from the
850 ubiquitous osmolyte glycine betaine in coastal saltmarsh sediments. *MICROBIOME* **7**.

851 Kaznatcheev K. V, Karunakaran C., Lanke U. D., Urquhart S. G., Obst M. and Hitchcock A. P.
852 (2007) Soft X-ray spectromicroscopy beamline at the CLS: commissioning results. *Nucl.*
853 *Instruments Methods Phys. Res. Sect. A Accel. Spectrometers, Detect. Assoc. Equip.* **582**,
854 96–99.

855 Keiluweit M., Wanzek T., Kleber M., Nico P. and Fendorf S. (2017) Anaerobic microsites have
856 an unaccounted role in soil carbon stabilization. *Nat. Commun.* **8**.

857 Kelley C. A., Martens C. S., Iii W. U., Sciences M., Hall V., No C. B., Kelley A. and Martens S.
858 (1995) Methane dynamics across a tidally flooded riverbank margin. *Am. Soc. Limnol.*
859 *Oceanogr.* **40**, 1112–1129.

860 King G. M. (1984) Metabolism of trimethylamine, choline, and glycine betaine by sulfate-
861 reducing and methanogenic bacteria in marine sediments. *Appl. Environ. Microbiol.* **48**,
862 719–725.

863 King G. M. and Wiebe W. J. (1978) Methane release from soils of a Georgia salt-marsh.
864 *Geochim. Cosmochim. Acta* **42**, 343–348.

865 Kinyangi J., Solomon D., Liang B., Lerotic M., Wirick S. and Lehmann J. (2006) Nanoscale

866 biogeocomplexity of the organomineral assemblage in soil. *Soil Sci. Soc. Am. J.* **70**, 1708–
867 1718.

868 Kludze H. K., Delaune R. D. and Patrick W. H. (1993) Aerenchyma formation and methane and
869 oxygen-exchange in rice . *Soil Sci. Soc. Am. J.* **57**, 386–391.

870 Knittel K. and Boetius A. (2009) Anaerobic Oxidation of Methane: Progress with an Unknown
871 Process. *Annu. Rev. Microbiol.* **63**, 311–334.

872 Knox S. H., Jackson R. B., Poulter B., McNicol G., Fluet-Chouinard E., Zhang Z., Hugelius G.,
873 Bousquet P., Canadell J. G., Saunois M., Papale D., Chu H., Keenan T. F., Baldocchi D.,
874 Torn M. S., Mammarella I., Trotta C., Aurela M., Bohrer G., Campbell D. I., Cescatti A.,
875 Chamberlain S., Chen J., Chen W., Dengel S., Desai A. R., Euskirchen E., Friborg T.,
876 Gasbarra D., Goded I., Goeckede M., Heimann M., Helbig M., Hirano T., Hollinger D. Y.,
877 Iwata H., Kang M., Klatt J., Krauss K. W., Kutzbach L., Lohila A., Mitra B., Morin T. H.,
878 Nilsson M. B., Niu S., Noormets A., Oechel W. C., Peichl M., Peltola O., Reba M. L.,
879 Richardson A. D., Runkle B. R. K., Ryu Y., Sachs T., Schäfer K. V. R., Schmid H. P.,
880 Shurpali N., Sonnentag O., Tang A. C. I., Ueyama M., Vargas R., Vesala T., Ward E. J.,
881 Windham-Myers L., Wohlfahrt G. and Zona D. (2019) FLUXNET-CH_4 Synthesis Activity:
882 Objectives, Observations, and Future Directions. *Bull. Am. Meteorol. Soc.* **0**, BAMS-D-18-
883 0268.1. Available at: http://journals.ametsoc.org/doi/10.1175/BAMS-D-18-0268.1.

884 Kristjansson J. K., Schönheit P. and Thauer R. K. (1982) Different Ks values for hydrogen of
885 methanogenic bacteria and sulfate reducing bacteria: An explanation for the apparent
886 inhibition of methanogenesis by sulfate. *Arch. Microbiol.* **131**, 278–282.

887 Kuivila K. M., Murray J. W., Devol A. H. and Novelli P. C. (1989) Methane production, sulfate

reduction and competition for substrates in the sediments of Lake Washington. *Geochim. Cosmochim. Acta* **53**, 409–416.

LaCroix R. E., Tfaily M. M., McCreight M., Jones M. E., Spokas L. and Keiluweit M. (2019) Shifting mineral and redox controls on carbon cycling in seasonally flooded mineral soils. *BIOGEOSCIENCES* **16**, 2573–2589.

LaForce M. J., Hansel C. M. and Fendorf S. (2000) Constructing Simple Wetland Sampling Devices. *Soil Sci. Soc. Am. J.* **64**, 809.

Lerotic M., Jacobsen C., Gillow J. B., Francis A. J., Wirick S., Vogt S. and Maser J. (2005) Cluster analysis in soft X-ray spectromicroscopy: Finding the patterns in complex specimens. *J. Electron Spectros. Relat. Phenomena* **144–147**, 1137–1143.

Liu L., Wang D., Chen S., Yu Z., Xu Y., Li Y., Ge Z. and Chen Z. (2019) Methane Emissions from Estuarine Coastal Wetlands: Implications for Global Change Effect. *SOIL Sci. Soc. Am. J.* **83**, 1368–1377.

Lovley D. R. and Phillips E. J. (1987) Competitive mechanisms for inhibition of sulfate reduction and methane production in the zone of ferric iron reduction in sediments. *Appl. Environ. Microbiol.* **53**, 2636–41.

Magenheimer J. F., Moore T. R., Chmura G. L. and Daoust R. J. (1996) Methane and carbon dioxide flux from a macrotidal salt marsh, Bay of Fundy, New Brunswick. *ESTUARIES* **19**, 139–145.

Maher D. T., Cowley K., Santos I. R., Macklin P. and Eyre B. D. (2015) Methane and carbon dioxide dynamics in a subtropical estuary over a diel cycle: Insights from automated in situ

radioactive and stable isotope measurements. *Mar. Chem.* **168**, 69–79.

Marschner H. (2003) *Mineral Nutrition of Higher Plants*. 2nd ed., Academic Press, New York.

Martens C. S. and Berner R. A. (1977) Interstitial water chemistry of anoxic Long Island Sound sediments. 1. Dissolved gases. *Limnol. Oceanogr.* **22**, 10–25.

Masue-Slowey Y., Kocar B. D., Jofre S. A. B., Mayer K. U. and Fendorf S. (2011) Transport Implications Resulting from Internal Redistribution of Arsenic and Iron within Constructed Soil Aggregates. *Environ. Sci. Technol.* **45**, 582–588.

McKeague J. a. and Day J. H. (1966) Dithionite- and oxalate-extractable Fe and Al as aids in differentiating various classes of soils. *Can. J. Soil Sci.* **46**, 13–22.

Mcleod E., Chmura G. L., Bouillon S., Salm R., Bjork M., Duarte C. M., Lovelock C. E., Schlesinger W. H. and Silliman B. R. (2011) A blueprint for blue carbon: toward an improved understanding of the role of vegetated coastal habitats in sequestering CO2. *Front. Ecol. Environ.* **9**, 552–560.

Mcowen C. J., Weatherdon L. V, Van Bochove J.-W., Sullivan E., Blyth S., Zockler C., Stanwell-Smith D., Kingston N., Martin C. S., Spalding M. and Fletcher S. (2017) A global map of saltmarshes. *Biodivers. DATA J.* **5**.

Mehra O. P. (1958) Iron Oxide Removal from Soils and Clays by a Dithionite-Citrate System Buffered with Sodium Bicarbonate. *Clays Clay Miner.* **7**, 317–327.

Mer J. Le and Roger P. (2010) Production, oxidation, emission and consumption of methane by soils : A review. *Eur. J. Soil Sci.* **37**, 25–50.

929 Middelburg J. J., Nieuwenhuize J., Iversen N., Høgh N., Wilde H. De, Helder W., Seifert R.,
930 Christof O., Helder W. I. M., Hogh N. and Wilde H. D. E. (2014) Methane distribution in
931 European tidal estuaries. *Biogeochemistry* **59**, 95–119.

932 Mikutta R., Kleber M., Torn M. S. and Jahn R. (2006) Stabilization of soil organic matter:
933 Association with minerals or chemical recalcitrance? *Biogeochemistry* **77**, 25–56.

934 Montalto F. a., Parlange J.-Y. and Steenhuis T. S. (2007) A simple model for predicting water
935 table fluctuations in a tidal marsh. *Water Resour. Res.* **43**.

936 Moore T. and Dalva M. (1993) The influence of temperature and water table position on carbon
937 dioxide and methane emissions from laboratory columns of peatland soils. *Eur. J. Soil Sci.*
938 **44**, 651–664.

939 Moore T. and Roulet N. (1993) Methane flux: water table relations in northern wetlands.
940 *Geophys. Res. Lett.* **20**, 587–590.

941 Morse J. W., Millero F. J., Cornwell J. C. and Rickard D. (1987) The chemistry of the hydrogen
942 sulfide and iron sulfide systems in natural waters. *Earth Sci. Rev.* **24**, 1–42.

943 Van Der Nat F.-J. and Middelburg J. J. (2000) Methane Emission from Tidal Freshwater
944 Marshes. *Biogeochemistry* **49**, 103–121.

945 Nestler J. (1977a) A preliminary study of the sediment hydrology of a Georgia salt marsh using
946 Rhodamine WT as a tracer. *Southeast. Geol.* **18**, 265–271.

947 Nestler J. (1977b) Interstitial salinity as a cause of ecophenic variation in Spartina alterniflora.
948 *Estuar. Coast. Mar. Sci.* **5**, 707–714.

949 Oremland R. S., Marsh L. M. and Polcin S. (1982) Methane production and simultaneous
950 sulphate reduction in anoxic, salt marsh sediments. *Nature* **296**, 143–145.

951 Pallud C., Masue-Slowey Y. and Fendorf S. (2010) Aggregate-scale spatial heterogeneity in
952 reductive transformation of ferrihydrite resulting from coupled biogeochemical and physical
953 processes. *Geochim. Cosmochim. Acta* **74**, 2811–2825.

954 Pearson A. J., Pizzuto J. E. and Vargas R. (2016) Influence of run of river dams on floodplain
955 sediments and carbon dynamics. *Geoderma* **272**, 51–63.

956 Pendleton L., Donato D. C., Murray B. C., Crooks S., Jenkins W. A., Sifleet S., Craft C.,
957 Fourqurean J. W., Kauffman J. B., Marba N., Megonigal P., Pidgeon E., Herr D., Gordon D.
958 and Baldera A. (2012) Estimating Global ``Blue Carbon{''} Emissions from Conversion
959 and Degradation of Vegetated Coastal Ecosystems. *PLoS One* **7**.

960 Penido E. S., Bennett A. J., Hanson T. E. and Seyfferth A. L. (2016) Biogeochemical impacts of
961 silicon-rich rice residue incorporation into flooded soils: Implications for rice nutrition and
962 cycling of arsenic. *Plant Soil* **399**.

963 Petrakis S., Seyfferth A., Kan J., Inamdar S. and Vargas R. (2017) Influence of experimental
964 extreme water pulses on greenhouse gas emissions from soils. *Biogeochemistry* **133**.

965 Petrescu A. M. R., Lohila A., Tuovinen J.-P., Baldocchi D. D., Desai A. R., Roulet N. T., Vesala
966 T., Dolman A. J., Oechel W. C., Marcolla B., Friborg T., Rinne J., Matthes J. H., Merbold
967 L., Meijide A., Kiely G., Sottocornola M., Sachs T., Zona D., Varlagin A., Lai D. Y. F.,
968 Veenendaal E., Parmentier F.-J. W., Skiba U., Lund M., Hensen A., van Huissteden J.,
969 Flanagan L. B., Shurpali N. J., Grünwald T., Humphreys E. R., Jackowicz-Korczyński M.,

970 Aurela M. A., Laurila T., Grüning C., Corradi C. A. R., Schrier-Uijl A. P., Christensen T.
971 R., Tamstorf M. P., Mastepanov M., Martikainen P. J., Verma S. B., Bernhofer C. and
972 Cescatti A. (2015) The uncertain climate footprint of wetlands under human pressure. *Proc.*
973 *Natl. Acad. Sci.* **112**, 4594 LP – 4599. Available at:
974 http://www.pnas.org/content/112/15/4594.abstract.

975 Phillips C. L., Bond-Lamberty B., Desai A. R., Lavoie M., Risk D., Tang J., Todd-Brown K. and
976 Vargas R. (2017) The value of soil respiration measurements for interpreting and modeling
977 terrestrial carbon cycling. *Plant Soil* **413**, 1–25.

978 Poffenbarger H. J., Needelman B. a. and Megonigal J. P. (2011) Salinity influence on methane
979 emissions from tidal marshes. *Wetlands* **31**, 831–842.

980 Postma D. and Jakobsen R. (1996) Redox zonation : Equilibrium constraints on the Fe (III)/
981 SO4-reduction interface. *Geochim. Cosmochica* **60**, 3169–3175.

982 Rasmussen C., Heckman K., Wieder W. R., Keiluweit M., Lawrence C. R., Berhe A. A.,
983 Blankinship J. C., Crow S. E., Druhan J. L., Pries C. E. H., Marin-Spiotta E., Plante A. F.,
984 Schadel C., Schimel J. P., Sierra C. A., Thompson A. and Wagai R. (2018) Beyond clay:
985 towards an improved set of variables for predicting soil organic matter content.
986 *Biogeochemistry* **137**, 297–306.

987 Rasmussen C., Southard R. J. and Horwath W. R. (2006) Mineral control of organic carbon
988 mineralization in a range of temperate conifer forest soils. *Glob. Chang. Biol.* **12**, 834–847.

989 Ravel B. and Newville M. (2005) ATHENA, ARTEMIS, HEPHAESTUS: data analysis for X-
990 ray absorption spectroscopy using IFEFFIT. *J. Synchrotron Radiat.* **12**, 537–541.

991 Reese B. K., Finneran D. W., Mills H. J., Zhu M.-X. and Morse J. W. (2011) Examination and
992 refinement of the determination of aqueous hydrogen sulfide by the methylene blue method.
993 *Aquat. Geochemistry* **17**, 567–582.

994 Reid M. C., Tripathee R., Schäfer K. V. R. and Jaffé P. R. (2013) Tidal marsh methane
995 dynamics: Difference in seasonal lags in emissions driven by storage in vegetated versus
996 unvegetated sediments. *J. Geophys. Res. Biogeosciences* **118**, 1802–1813.

997 Roulet N. T. (2000) Peatlands, carbon storage, greenhouse gases, and the Kyoto Protocol:
998 Prospects and significance for Canada. *WETLANDS* **20**, 605–615.

999 Rowley M. C., Grand S. and Verrecchia E. P. (2018) Calcium-mediated stabilisation of soil
1000 organic carbon. *Biogeochemistry* **137**, 27–49.

1001 Segarra K. E. A., Comerford C., Slaughter J. and Joye S. B. (2013) Impact of electron acceptor
1002 availability on the anaerobic oxidation of methane in coastal freshwater and brackish
1003 wetland sediments. *Geochim. Cosmochim. Acta* **115**, 15–30.

1004 Segers R. (1998) Methane production and methane consumption : a review of processes
1005 underlying wetland methane fluxes. *Biogeochemistry*, 23–51.

1006 Senior E., Lindstrom E. B., Banat I. M. and Nedwell D. B. (1982) c. *Appl. Environ. Microbiol.*
1007 **43**, 987–996.

1008 Silver W. L., Lugo A. E. and Keller M. (1999) Soil oxygen availability and biogeochemistry
1009 along rainfall and topographic gradients in upland wet tropical forest soils. *Biogeochemistry*
1010 **44**, 301–328.

1011 Smith K. A., Ball T., Conen K. E., Dobbiw J., Massheder J. and Rey A. (2003) Exchange of

greenhouse gases between soil and atmosphere : interactions of soil physical factors and biological processes. *Eur. J. Soil Sci.* **54**, 779–791.

Stookey L. L. (1970) Ferrozine---a new spectrophotometric reagent for iron. *Anal. Chem.* **42**, 779–781.

Teh Y. A. and Silver W. L. (2006) Effects of soil structure destruction on methane production and carbon partitioning between methanogenic pathways in tropical rain forest soils. *J. Geophys. Res.* **111**, G01003.

Ticak T., Hariraju D., Arcelay M. B., Arivett B. A., Fiester S. E. and Ferguson Jr. D. J. (2015) Isolation and characterization of a tetramethylammonium-degrading Methanococcoides strain and a novel glycine betaine-utilizing Methanolobus strain. *Arch. Microbiol.* **197**, 197–209.

Tong C., Huang J. F., Hu Z. Q. and Jin Y. F. (2013) Diurnal variations of carbon dioxide, methane, and nitrous oxide vertical fluxes in a subtropical estuarine marsh on neap and spring tide days. *Estuaries and Coasts* **36**, 633–642.

Trifunovic B., Lule A. V., Capooci M., Seyfferth A., Moffat C. F. and Vargas R. (2018) Patterns and Drivers of Carbon Dioxide and Methane Emissions from a Temperate Salt Marsh Creek. In *AGU Fall Meeting* American Geophysical Union, Washington, D.C. pp. B43-2928.

Trotsenko Y. A. and Murrell J. C. (2008) Metabolic aspects of aerobic obligate methanotrophy. In *ADVANCES IN APPLIED MICROBIOLOGY, VOL 63* (ed. Laskin, AL and Sariaslani, S). Advances in Applied Microbiology. pp. 183–229.

1033 Vaksmaa A., Luke C., van Alen T., Vale G., Lupotto E., Jetten M. S. M. and Ettwig K. F. (2016)
1034 Distribution and activity of the anaerobic methanotrophic community in a nitrogen-
1035 fertilized Italian paddy soil. *Fems Microbiol. Ecol.* **92**.

1036 Villa J. A., Ju Y., Vines C., Rey-Sanchez C., Morin T. H., Wrighton K. C. and Bohrer G. (2019)
1037 Relationships between methane and carbon dioxide fluxes in a temperate cattail-dominated
1038 freshwater wetland. *J. Geophys. Res. Biogeosciences* **0**. Available at:
1039 https://agupubs.onlinelibrary.wiley.com/doi/abs/10.1029/2019JG005167.

1040 Wachinger G., Fiedler S., Zepp K., Gattinger A., Sommer M. and Roth K. (2000) Variability of
1041 soil methane production on the micro-scale: spatial association with hot spots of organic
1042 material and Archaeal populations. *Soil Biol. Biochem.* **32**, 1121–1130.

1043 Waddington J. M. and Roulet N. T. (1996) Atmosphere-wetland carbon exchanges: Scale
1044 dependency of CO2 and CH4 exchange on the developmental topography of a peatland.
1045 *Global Biogeochem. Cycles* **10**, 233–245.

1046 Wagai R. and Mayer L. M. (2007) Sorptive stabilization of organic matter in soils by hydrous
1047 iron oxides. *Geochim. Cosmochim. Acta* **71**, 25–35.

1048 Wan J., Tyliszczak T. and Tokunaga T. K. (2007) Organic carbon distribution, speciation, and
1049 elemental correlations within soil microaggregates: applications of STXM and NEXAFS
1050 spectroscopy. *Geochim. Cosmochim. Acta* **71**, 5439–5449.

1051 Wang X. C. and Lee C. (1994) Sources and distribution of aliphatic amines in salt marsh
1052 sediment. *Org. Geochem.* **22**, 1005–1021.

1053 Warner D. L., Vargas R., Seyfferth A. and Inamdar S. (2018) Transitional slopes act as hotspots

of both soil CO<inf>2</inf>emission and CH<inf>4</inf>uptake in a temperate forest landscape. *Biogeochemistry* **138**.

Watkins A. J., Roussel E. G., Parkes R. J. and Sass H. (2014) Glycine Betaine as a Direct Substrate for Methanogens (Methanococcoides spp.). *Appl. Environ. Microbiol.* **80**, 289–293.

Weston N. B., Dixon R. E. and Joye S. B. (2006) Ramifications of increased salinity in tidal freshwater sediments: Geochemistry and microbial pathways of organic matter mineralization. *J. Geophys. Res.* **111**, G01009.

Weston N. B., Vile M. a., Neubauer S. C. and Velinsky D. J. (2010) Accelerated microbial organic matter mineralization following salt-water intrusion into tidal freshwater marsh soils. *Biogeochemistry* **102**, 135–151.

Wiegert R. G. and Freeman B. J. (1990) *Tidal salt marshes of the Southeastern Atlantic coast: A community profile.*, Washington, D.C.

Wilson B. J., Mortazavi B. and Kiene R. P. (2015) Spatial and temporal variability in carbon dioxide and methane exchange at three coastal marshes along a salinity gradient in a northern Gulf of Mexico estuary. *Biogeochemistry* **123**, 329–347.

Winfrey M. R. and Zeikus J. G. (1977) Effect of sulfate on carbon and electron flow during microbial methanogenesis in Effect of Sulfate on Carbon and Electron Flow During Microbial Methanogenesis in Freshwater Sediments. *Apploed Environ. Microbiol.* **33**, 275.

Wolanski E. (2007) *Estuarine Ecohydrology*. 1st ed., Elsevier, Oxford, UK.

Xiao K.-Q., Beulig F., Kjeldsen K. U., Jorgensen B. B. and Risgaard-Petersen N. (2017)

1075 Concurrent Methane Production and Oxidation in Surface Sediment from Aarhus Bay,
1076 Denmark. *Front. Microbiol.* **8**.

1077 Xiao K.-Q., Beulig F., Roy H., Jorgensen B. B. and Risgaard-Petersen N. (2018) Methylotrophic
1078 methanogenesis fuels cryptic methane cycling in marine surface sediment. *Limnol.*
1079 *Oceanogr.* **63**, 1519–1527.

1080 Yang S. S. and Chang H. L. (1998) Effect of environmental conditions on methane production
1081 and emission from paddy soil. *Agric. Ecosyst. Environ.* **69**, 69–80.

1082 Ying S. C., Masue-Slowey Y., Kocar B. D., Griffis S. D., Webb S., Marcus M. A., Francis C. A.
1083 and Fendorf S. (2013) Distributed microbially- and chemically-mediated redox processes
1084 controlling arsenic dynamics within Mn-/Fe-oxide constructed aggregates. *Geochim.*
1085 *Cosmochim. Acta* **104**, 29–41.

1086 Yuan J., Liu D., Ji Y., Xiang J., Lin Y., Wu M. and Ding W. (2019) Spartina alterniflora
1087 invasion drastically increases methane production potential by shifting methanogenesis
1088 from hydrogenotrophic to methylotrophic pathway in a coastal marsh. *J. Ecol.* **107**, 2436–
1089 2450.

1090

Figures

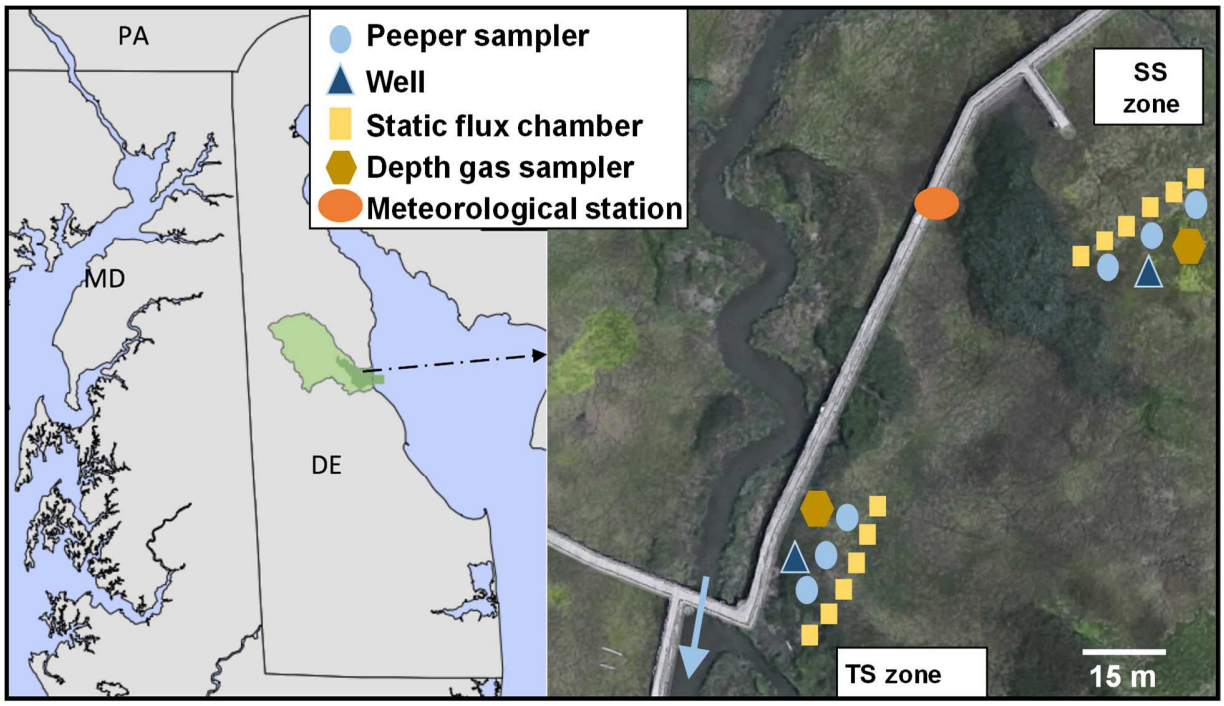

Figure 1. Study site location at the St. Jones Reserve near Dover, DE. Map of Delaware and surrounding states with the St. Jones River watershed highlighted in light green (left), and a Google image showing the Tall *Spartina* (TS) and Short *Spartina* (SS) vegetation zones equipped with water and gas sampling devices (right). The arrow represents the outgoing flow of tidal channel water.

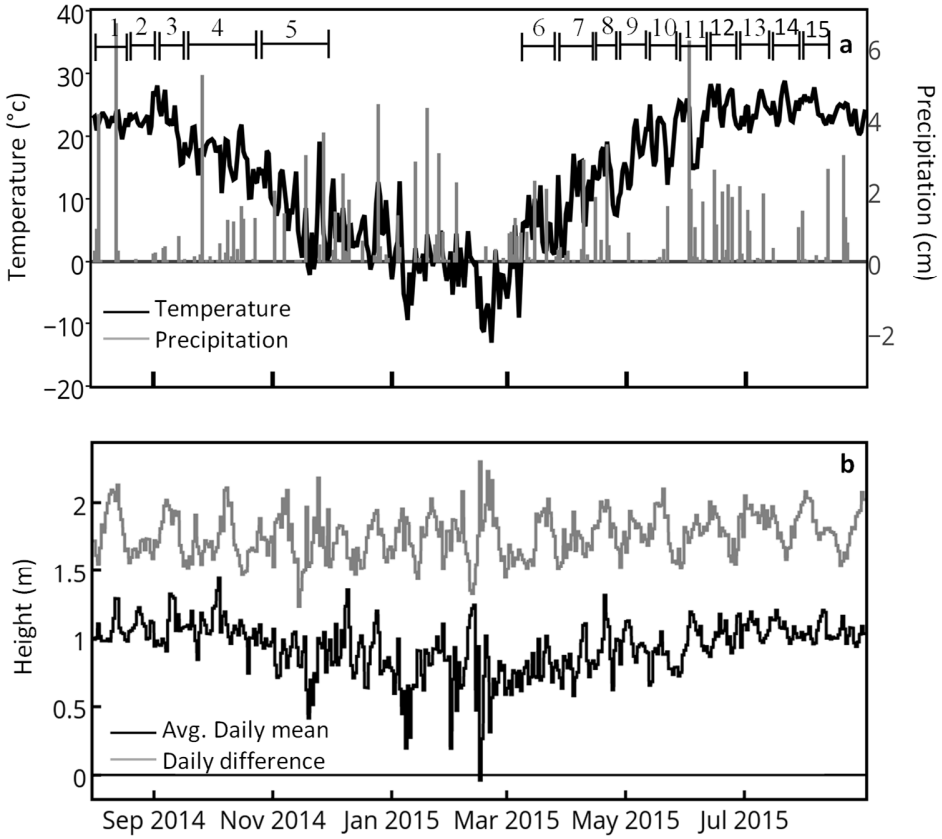

Figure 2. Average daily temperature (black) and precipitation (grey) at the St. Jones Reserve over the 15 sampling periods labeled 1-15 (a) and average daily mean (black) and daily difference between high and low tide (grey) in the St. Jones River (b). Numbers 1-15 in panel (a) correspond to equilibrium time for peeper sampling events reported in Figure 3 and Supporting Figure S3.

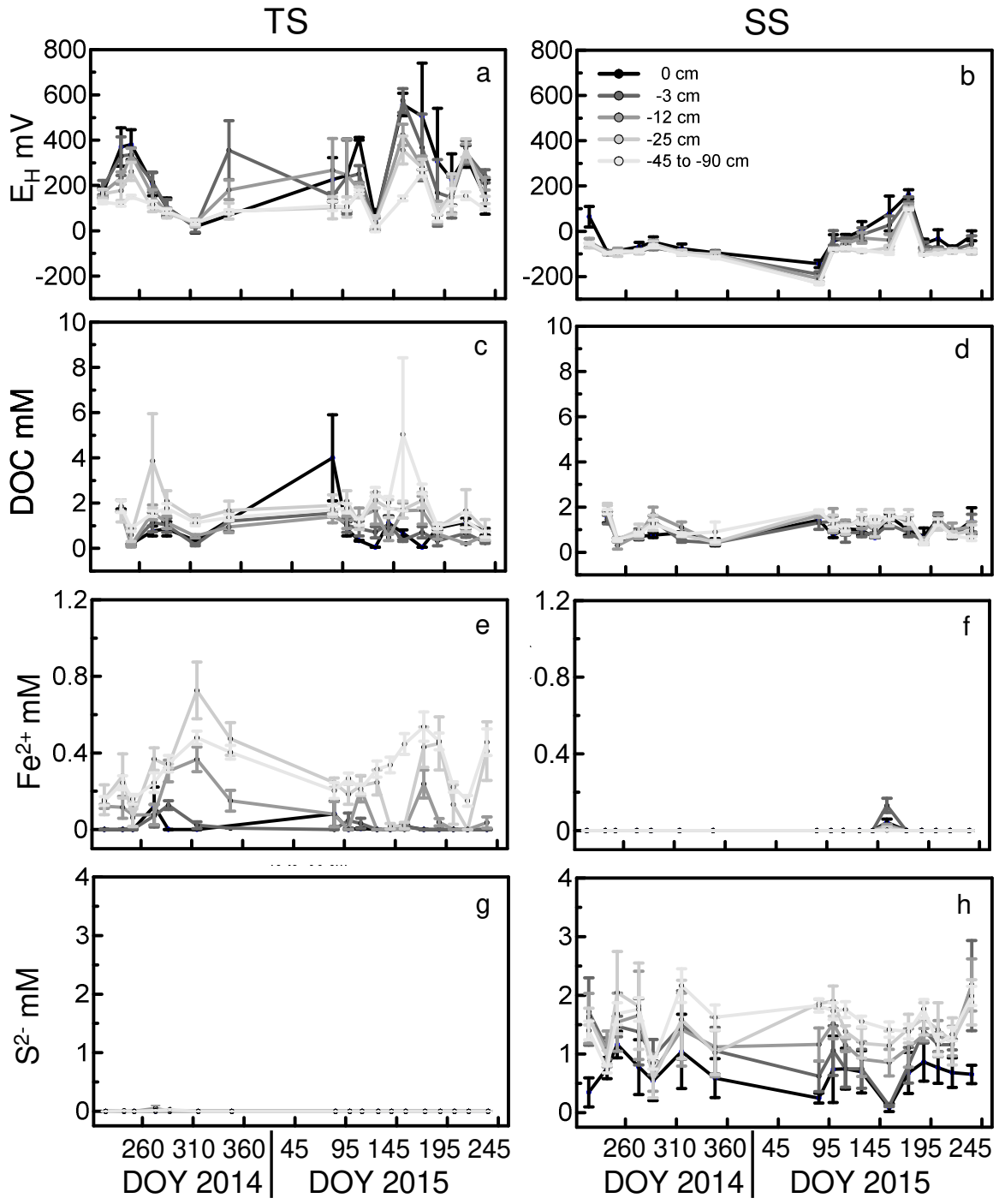

Fig 3. Average (±SE, *n*=3) porewater redox potential (a, b), DOC (c, d), ferrous iron (e, f), and sulfide (g, h) measured in 2014-2015 for both TS (a, c, e, g) and SS (b, d, f, h) zones.

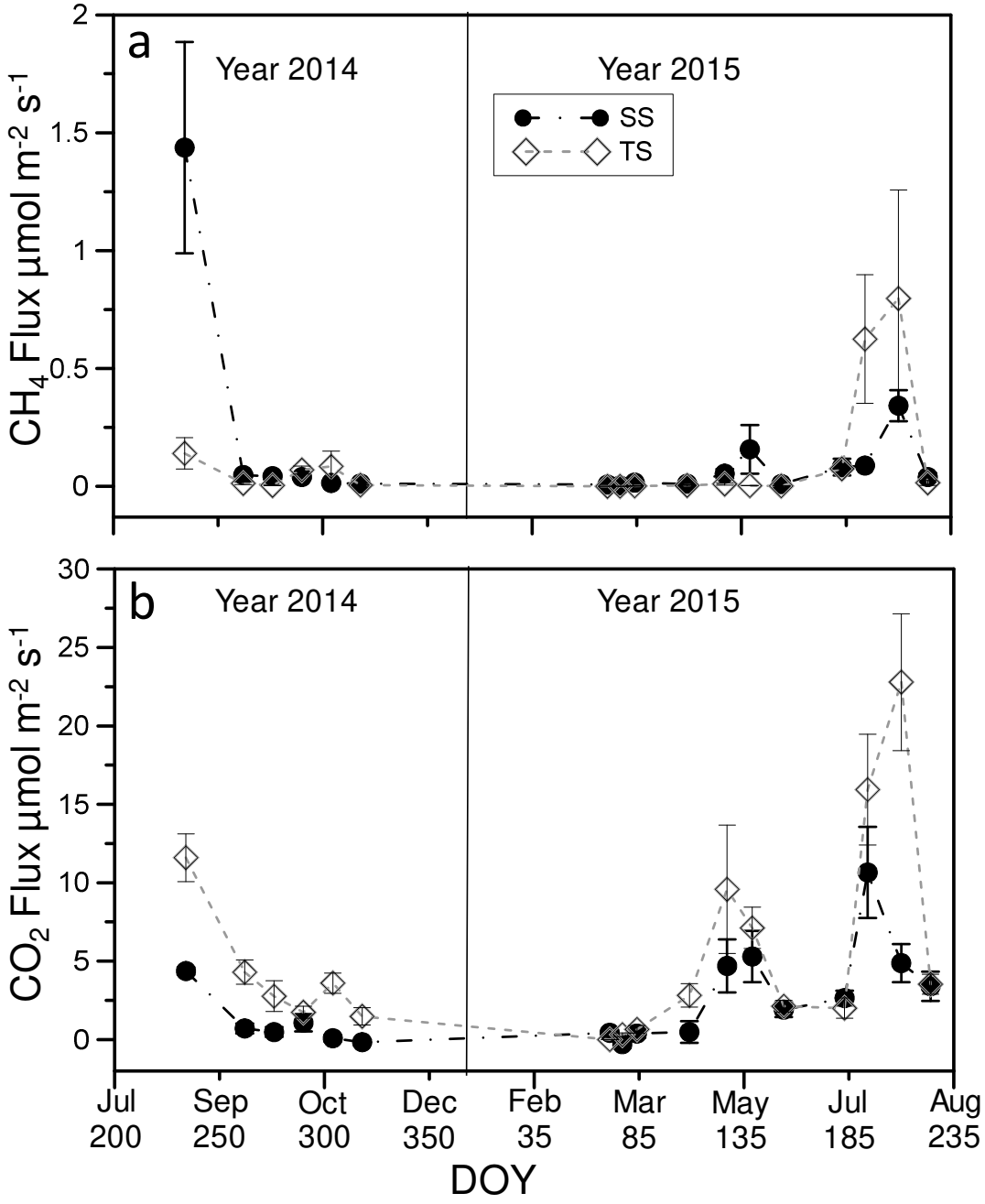

Fig 4. Average (±SE, *n*=6) flux of CH_4 (a) and CO_2 (b) from a nest of 6 static flux chambers at the TS (open symbols) and SS (closed symbols) vegetation zones.

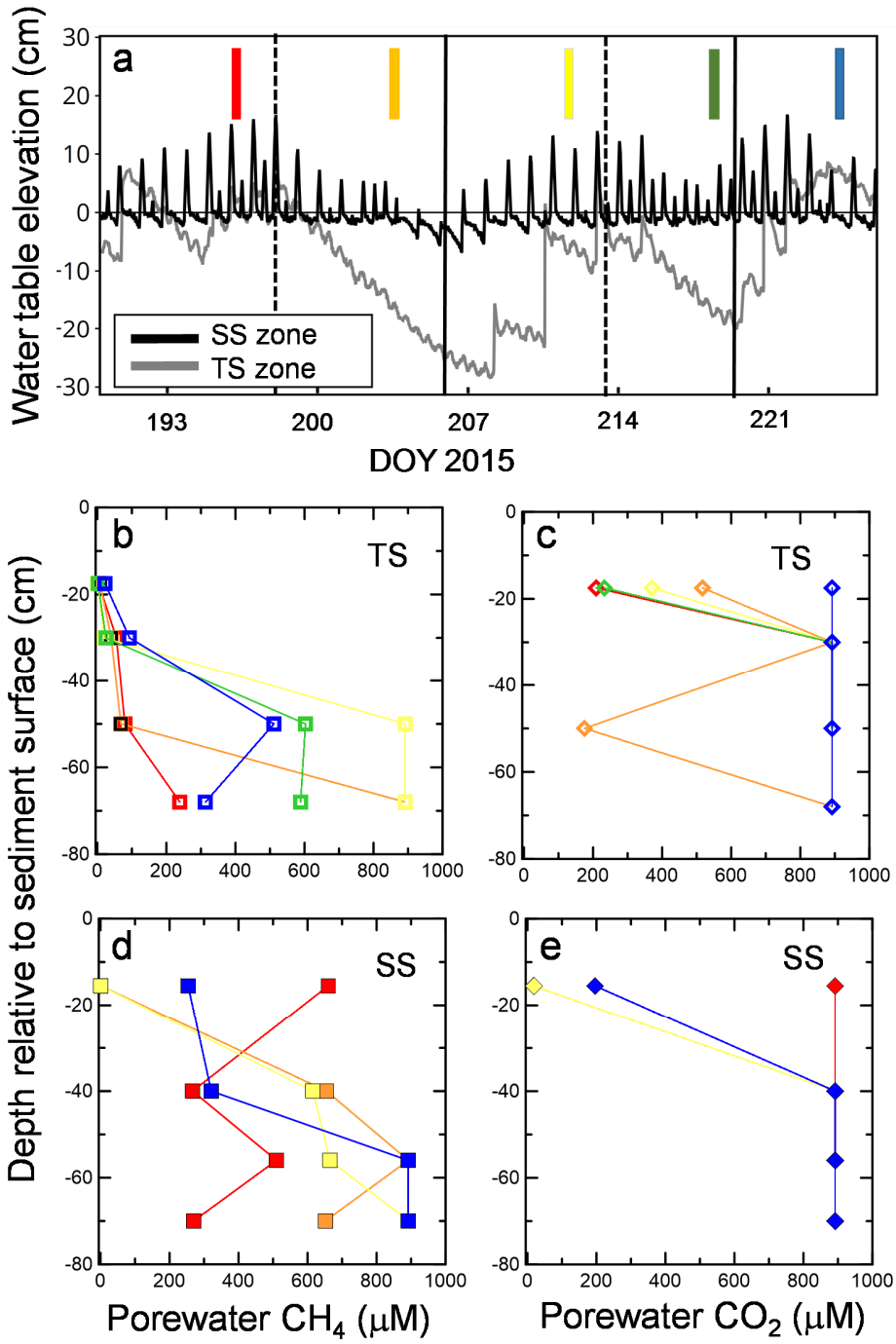

Figure 5. Water table elevations (a) at the SS (black) and TS (grey) vegetation zones during the summer 2015 sampling period where vertical lines indicate spring (dotted) and neap (solid) tides. Zero is marsh surface elevation. Colored bars in (a) indicate when depth profiles of CH_4 (b, d) and CO_2 (c,e) concentrations in equilibrium with sediment porewater were obtained with the depth profilers at the TS (open symbols) and SS (closed symbols) zones (n = 1 per zone). Note that the maximum value obtainable by the LGR instrument was 892 µM.

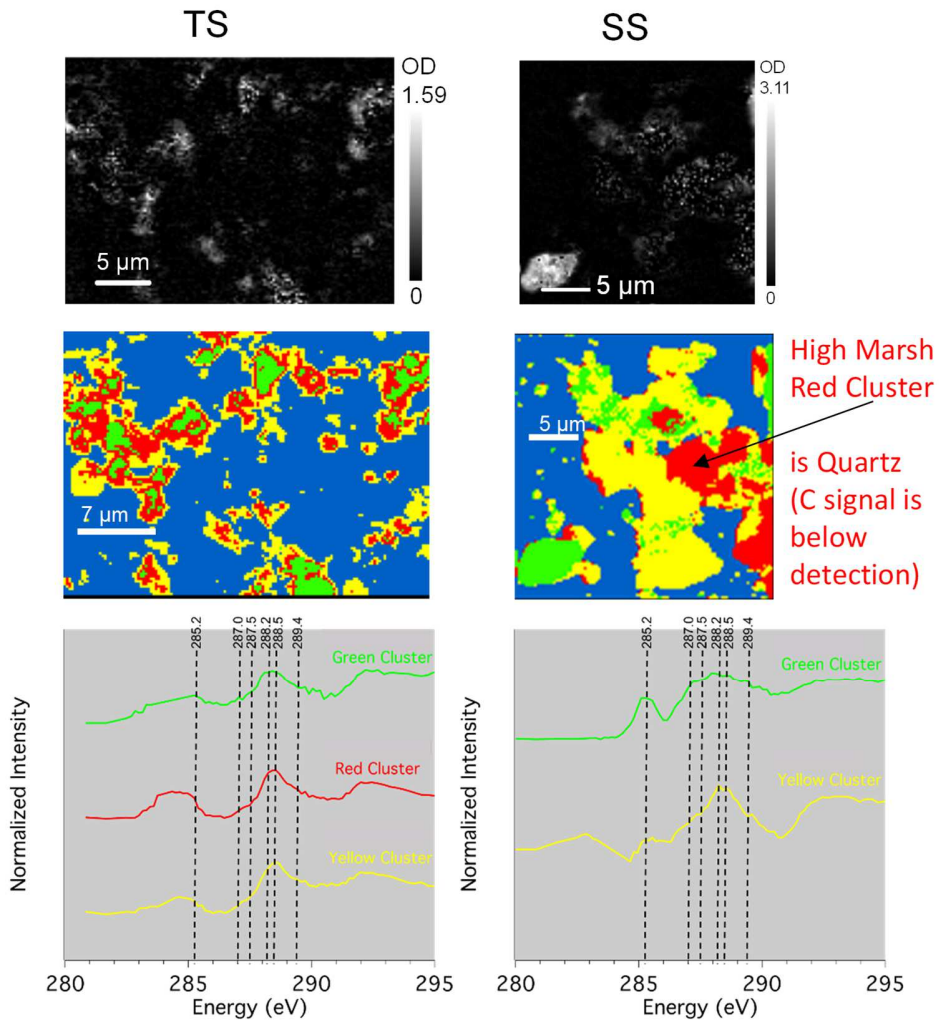

Figure 6. STXM C images, PCA analyses and NEXAFS data of sediment collected from 50 cm depth at TS and 56 cm at SS showing three components that consisted mainly of similar C functional groups at TS and distinct C functional groups and quartz at SS. Dashed vertical lines represent aromatic C at 285.2 eV, phenolic C at 287.0 eV, aliphatic C at 287.5 eV, carboxylamides at 288.2 eV, carboxylic C at 288.5 eV, and O-alkyl C at 289.4 eV.

TABLES

Table 1. Soil chemical properties of composite sediment horizons at the SS and TS zones at the St. Jones Reserve. AAO = ammonium oxalate extractable; CBD = citrate-bicarbonate-dithionite extractable.

Depth below surface (cm)	pH	%C	%N	%S	$BaCl_2$ Ca mmol kg^{-1}	AAO Fe mmol kg^{-1}	CBD Fe mmol kg^{-1}
	SS zone						
0-19	2.9	5.2	0.3	2.4	22	212	11
19-38	2.7	4.7	0.3	2.3	20	228	10
38-50	2.8	5.2	0.4	1.3	19	201	15
50-66	4.3	33.3	1.8	2.6	33	110	14
66-89	5.7	40.4	1.8	2.8	58	44	5
	TS zone						
0-27	4.7	14.1	0.8	1.9	16	152	14
27-73	3.3	8.6	0.6	2.4	14	196	11
73-89	3.6	8.6	0.7	2.2	12	298	10

Table 2. Linear combination fitting results of first shell Fe EXAFS spectra of sediment collected from four depths at the SS zone and three depths at the TS zone at the St. Jones Reserve. FHY = ferrihydrite; GOE = goethite; MAC = mackinawite; SID = siderite; PYR = pyrite; VIV = vivianite.

X-ray sample	depth below surface (cm)	----------% fitted species----------						Reduced χ^2	R value
		FHY	GOE	MAC	SID	PYR	VIV		
SS									
a	7	45	0.3	19	2.2	18	14	1.4	0.20
b	30	48	3.2	-	1.2	22	26	1.2	0.21
c	50	38	8.5	-	0.9	26	26	1.3	0.20
d	70	33	13	-	4.9	38	11	2.1	0.19
TS									
A	10	33	13	-	4.9	38	11	2.1	0.19
B	30	45	9.3	-	4.4	19	22	1.5	0.27
C	80	39	9.3	-	4.4	33	14	1.5	0.20